Nuclear Science and Techniques (2024) 35:216
https://doi.org/10.1007/s41365-024-01588-x

Clustering in nuclei: progress and perspectives

Kang Wei[1] · Yan-Lin Ye[1] · Zai-Hong Yang[1]

Received: 29 July 2024 / Revised: 29 September 2024 / Accepted: 30 September 2024 / Published online: 28 November 2024

Abstract
Nucleus is essentially composed of protons and neutrons, which are commonly known as nucleons. Interestingly, some of nucleons may group together and exhibit collective behavior inside a nucleus. Such clustering effects have been known since the early stages of nuclear physics because of the observation and description of α-cluster decay from many heavy nuclei. Subsequent studies demonstrated that cluster structures exist in many nuclear systems, especially in weakly bound or excited states, and are complementary to the shell-like structures. In this review article, we provide a brief historical recall of the field, and follow it with a conceptual and logical description of the major theoretical models that have been frequently applied in the literature to describe nuclear clustering. Experimental methods and progress are outlined, recent outcomes are emphasized, and perspectives relevant to future studies of heavy neutron-rich systems are discussed.

Keywords Nuclear matter · Cluster structure · Wave-packet presentation · Molecular bond · Condensation configuration

1 Introductory and historical view of nuclear clustering

Clustering is a general phenomenon that appears at every hierarchical layer of the matter universe, including the largest star systems [1] and the smallest hadron systems [2]. In nuclear systems, clustering commonly occurs in light nuclei, at the surface of heavy nuclei (e.g., α-particle formation and decay), and in weakly-bound or excited nuclei [3–6], as illustrated in Fig. 1. Clustering in many-body systems results from local few-body correlations becoming stronger than overall central interactions. Hence, clustering leads to fundamental changes in the motion regulation and main structural degree-of-freedom [7].

Before the discovery of the neutron in 1932, the α-particle was considered to be one of the basic constituents of the atomic nucleus, as given by the then well-known α-decay phenomenon [8, 9]. Following the recognition of the proton-neutron composition in the nucleus and the initialization of the independent-particle concept for nuclear structure in the 1930s [10], the α-cluster model continued to be one of the main approaches for describing nuclear structure [10, 11]. The microscopic basis for nuclear clustering, including the full antisymmetrization among all protons or neutrons, was originally introduced through the famous resonating group method (RGM) [12], and this was followed by its variants, including the generator coordinate method (GCM) [13] and orthogonal condition model (OCM) [14]. Notably, the explicit delineation of the coordinates collecting the center of mass (c.m.) of the clusters (groups) allows for the description of the collective cluster motion controlled by the effective interaction among them [15–17]. The importance of the nuclear clustering was highlighted by the discovery of the 7.65 MeV (0^+_2) state in ^{12}C, known as the Hoyle state, which exhibits a characteristic 3α cluster configuration and plays a crucial role in the synthesis of elements across carbon in stars [18–20].

Since the 1960s, studies on nuclear clustering were revived along with the occurrence of some exotic

Dedicated to Professor Wenqing Shen in honour of his 80th birthday.

This work was supported by the National Key R&D Program of China (Nos. 2023YFA1606403, 2023YFE0101600, 2022YFA1605100, and 2023YFE0101500) and the National Natural Science Foundation of China (Nos. 12027809, 11961141003, and 12275006).

✉ Yan-Lin Ye
yeyl@pku.edu.cn

✉ Zai-Hong Yang
zaihong.yang@pku.edu.cn

[1] School of Physics and State Key Laboratory of Nuclear Physics and Technology, Peking University, Beijing 100871, China

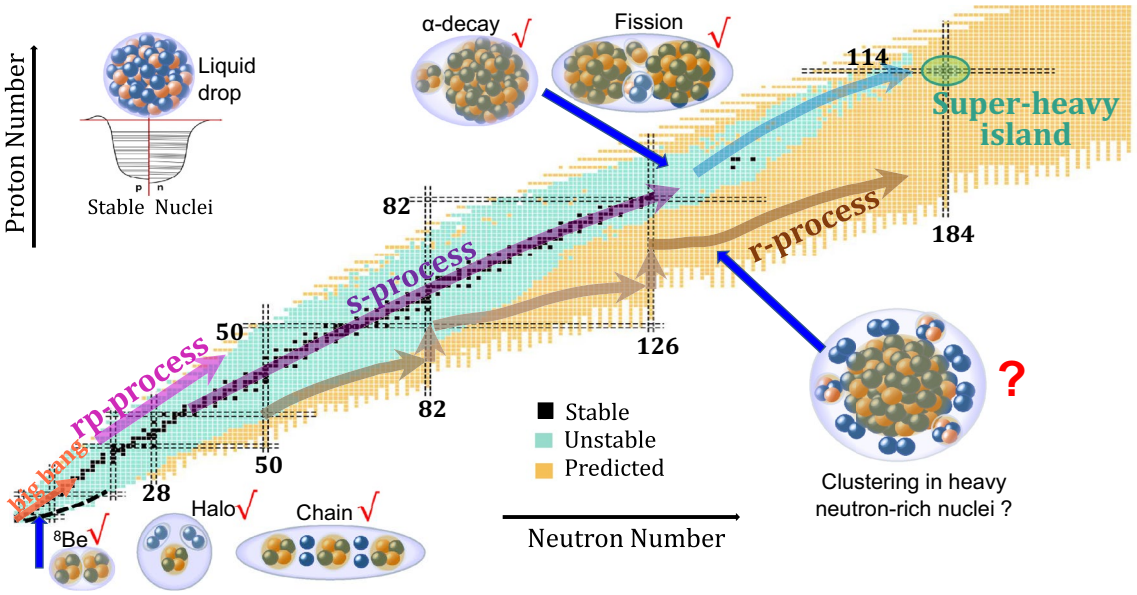

Fig. 1 (Color online) Nuclear chart and illustration of clustering in nuclei. The observed stable (black squares) and unstable (blue squares) nuclei [5] as well as the predicted nuclides (yellow squares) [6] are symbolized. The thick arrows on the landscape indicate the major processes for the creation of elements in the cosmos, or the way toward the superheavy element island. Representative nuclear cluster structures are sketched in the inset images, with the symbol "✓" indicating structures that have already been experimentally confirmed and the "?" symbol indicating anticipated structures that warrant future exploration

excitation spectra that were inconsistent with single-particle picture of nuclei [21]. During this time, the wave-packet representation of a nuclear state, known as the Brink wave function (w.f.), was also proposed [22]. The Brink w.f. is particularly appropriate for describing clustering phenomena, considering its favorable model space, compared with that of the orbit-presentation, which is suitable for describing independent-particle motion in a centralized mean field. In 1968, the Ikeda diagram was introduced to indicating the favorable conditions for cluster formation in the vicinity of the corresponding cluster separation threshold [3, 23]. At the highest order of clustering, the Ikeda diagram gives rise to a pure α composition for α-conjugate nuclei. If all α-particles move in relative s-waves, then the Bose–Einstein condensation (BEC) can be adopted to characterize the nuclear system, as represented by the Tohsaki–Horiuchi–Schuck–Röpke (THSR) w.f. [24, 25]. The Hoyle state is an example of such a BEC-like state [15, 19, 26]. However, despite recent, remarkable advancements in theoretical predictions [27], the experimental determination of BEC-like states is still limited. The latest report on the experimental observation of Hoyle-like resonances in ^{16}O [28] is encouraging regarding the further exploration of condensation states in heavier α-conjugate nuclei. Notably, the Ikeda diagram was extended to systems with excessive valence neutrons or protons, in addition to cluster cores, which gave rise to more abundant threshold arrangements associated with the formation of the molecular structures [3, 29, 30]. These topics will be further addressed in the following.

Over the past three decades, nuclear physics has entered into a new era of exploring the largely expanded nuclear chart away from the β-stability line [3, 4, 31]. Several theoretical approaches were further developed to investigate various aspects of nuclear clustering in unstable nuclei, including the antisymmetrized molecular dynamics (AMD) and fermion molecular dynamics (FMD) models [32–35] as well as the container model extended from the THSR w.f. [27, 36–38]. These models employ the Brink-type wave-packet representation and start from the nucleon degree of freedom with full antisymmetrization to cover the major cluster features from the microscopic basis. Another category of models assumes cluster formation a priori and concentrates on the role of valence nucleons, which may form various molecular bonds, such as the molecular orbital (MO) model [3, 39] and the generalized two-center cluster model (GTCM) [40]. Efforts were also made to apply single-particle-type or collective-vibration-type frameworks to account for clustering phenomena [41–43]. Thus far, the experimentally identified molecular structures in unstable nuclei are still quite limited and concentrated on light nuclei, such as neutron-rich beryllium and carbon isotopes [28, 44–50], as illustrated in Fig. 1. Important progress has been made in recent years regarding linear chain molecular states in ^{14,16}C [49, 50]. These results imply the possible existence of extremely exotic structures, such as ring configurations in heavy, neutron-rich nuclei

[51]. Another interesting phenomenon is the possible emergence of the compact two-neutron cluster (dineutron, ^{2}n) in low-density environments, which may largely affect the structures of neutron-rich nuclei and even the inner crust layers of neutron stars [52–58]. The latest finding regarding the BEC-type ^{4}He + ^{2}n + ^{2}n structure in ^{8}He(0^+_2) [59, 60] is encouraging for the future exploration of the rich clustering configurations in heavy, neutron-rich nuclei (Fig. 1). Recently, Tanaka et al. measured α clusters at the surfaces of neutron-rich Sn isotopes using the quasi-free (p,pα) knock-out reaction and examined their isotopic dependence [61]. Their results provide direct experimental evidence for the existence of α clusters at the surfaces of heavy nuclei and thus provide a natural explanation for the source of α decay. This work also reveals an interesting interplay between the formation of α clusters and development of the neutron skin, which will further impact the constraints on one key parameter of the nuclear equation of state, namely, the density-dependence parameter of the symmetry energy [62–64].

Along with the perfection of the model and experimental findings, a number of physics concepts have been proposed and justified, including the threshold effect [23], strong nucleon correlations in a low-density environment that potentially lead to the appearance of BEC states [15, 16], wave-packet description of a nuclear system with configuration mixing [59, 65, 66], and orthogonality of the quantum states driven by the valence neutron occupancy [40, 65, 66].

We outline the major theoretical models that have been frequently applied in the literature by emphasizing their conceptual and logical connections in Sect. 2. The major experimental methods and observations are selectively described in Sect. 3. Further perspectives are given in Sect. 4.

2 Theoretical descriptions of nuclear clustering

Over the past six decades, the description of the cluster structure in nuclei has progressed along with the observations of various clustering phenomena. Here, we outline the major models that have been widely used in the field and are still active in many applications of current research on nuclear clustering.

2.1 Resonating group method

The RGM was proposed by Wheeler [12]. At that time, the nucleon- and cluster-based models were competing to account for the observed properties of nuclei. Within the RGM approach, nucleons in a nucleus are configured into many groups, with the number of groups and numbers of protons and neutrons in each group being defined in a selective way. The spin of each group is constrained such that all spins must sum to the total spin of the nucleus. In addition, different configurations can be added together to present the complete w.f. [12]. The RGM is distinguished by its definition of the c.m. of each group and the relative coordinates between these c.m. positions (inter-cluster coordinates), upon which the interactions between the groups (cluster interactions) and the w.f. for the group–c.m. distribution (cluster w.f.) can be defined. The real cluster w.f. (probability distribution of the groups) can then be obtained according to the standard energy minimizing method, assuming the known Hamiltonian, which is also configured in line with the group definitions. In general, RGM focuses on addressing the cluster interactions and the cluster w.f. while treating the internal interaction and structure of each cluster (group) as a known basis. Hence, the selection of the group configurations should not be arbitrary. Instead, the selection should be performed in accordance with the real structure possibilities, as reflected by the existing observations and solid predictions. Otherwise, the results from the calculation might be different from reality due to the limited knowledge of the interactions (Hamiltonian) and unavoidable truncation of the configuration possibilities (state space). The RGM provides a flexible means by which to describe a complex many-body system that can suitably mix single-particle-type and cluster-type structures for use with nuclei that are far from the β-stability line. However, their method of use is still an unsolved challenge associated with experimental hints, theoretical background knowledge, and physical understanding [15, 59]. In addition, the full anti-symmetrization among all neutrons or protons of a system would cause large difficulties in real calculations. This constraint could partially be relaxed via the selection of a simple group configuration and the application of numerical methods, such as the generator coordinate method.

Here, we use a simple example to illustrate the RGM application [15, 67]. A system with A nucleons can be divided into two clusters with A_1 and A_2 nucleons. Then, the corresponding RGM w.f. can be expressed as:

$$\Phi(A_1, A_2, \boldsymbol{r}) = \mathcal{A}\chi(\boldsymbol{r})\phi(A_1)\phi(A_2), \tag{1}$$

Where the relative coordinate $\boldsymbol{r} = \boldsymbol{X}_{A_1} - \boldsymbol{X}_{A_2}$, with $\boldsymbol{X}_{A_1} = (1/A_1)\sum_{i=1}^{A_1}\boldsymbol{r}_i$ and $\boldsymbol{X}_{A_2} = (1/A_2)\sum_{i=1}^{A_2}\boldsymbol{r}_i$ being the c.m. coordinates of the two ingredient clusters A_1 and A_2, respectively. Here, $\mathcal{A}$ is the anti-symmetrization operator for all nucleons. The internal w.f.s $\phi(A_1)$ and $\phi(A_2)$ are presolved, using, e.g., in the harmonic oscillator single-particle model, which is represented only by its internal coordinates. The w.f. $\chi(\boldsymbol{r})$ that governs the relative motion between the clusters can be determined via the application of the energy variation principle after configuring the Hamiltonian as the

internal terms and a relative motion term [15]. In this framework, it is necessary to define the internal coordinates for each cluster:

$$\begin{aligned}\boldsymbol{\xi_{1i}} &= \boldsymbol{r}_i - \boldsymbol{X}_{A_1}, \quad i = 1, \ldots, A_1, \\ \boldsymbol{\xi_{2i}} &= \boldsymbol{r}_i - \boldsymbol{X}_{A_2}, \quad i = A_1 + 1, \ldots, A.\end{aligned} \tag{2}$$

Numerous studies have applied RGM, including those that examined the 3α configuration of the Hoyle state in ^{12}C [19]; X + ^{16}O configurations for ^{17}O, ^{18}F, ^{19}F, and ^{20}Ne [68, 69]; α + ^{6}He configuration for ^{10}Be [70]. One example for dripline nuclei can be found in Ref. [59], in which the extremely neutron-rich nucleus ^{8}He is configured as both ^{6}He(shell-like) + $2n^*$ (dissociable $2n$ cluster) and ^{4}He(shell-like) + $2n^*$ + ^{2}n(dineutron). After the energy minimization calculation, the dineutron-condensation-like structure is well revealed in the 0^+_2 state of ^{8}He, which gives rise to an important instruction for upcoming experiments [60].

2.2 Generator coordinate method

The GCM was originally proposed by Griffin and Wheeler to address the collective motion of the nuclear system [13]. This method aims to address overall coordinates, such as the deformation parameter of a nucleus, at several discrete values to generate the basis of the structure w.f.. These basis w.f. are then weighted and summed (integrated) to represent the structure w.f. for the system. The unknown weight factors, as a function of the generator coordinate, are determined according to the variational principle under the operation of the appropriate Hamiltonian. Hence, the complex calculations using the continuous variations of the dynamic coordinates can be simplified and extended to relatively heavier systems.

The GCM has naturally been combined with the RGM by using the inter-cluster coordinates as the generator coordinates [67, 71]. In the case of $^{9-11}$Be nuclei, the analysis using GCM reveals a decrease of the α-cluster contents from ^{9}Be to ^{11}Be. In addition, the results of this analysis predict a strong mixing of the ^{6}He + ^{6}He and ^{4}He + ^{8}He configurations in ^{12}Be nuclei. Recently, the combination of RGM and GCM has become the fashion for studying the structural configurations of nuclei far from the β-stability line. An exemplar is presented in Ref. [59], which demonstrates a case of ^{2}n clustering ^{8}He. The w.f. of the 0^+ states (^{8}He) is given in terms of the RGM + GCM:

$$\begin{aligned}\Psi_{^8\mathrm{He}(0^+)} = &\sum_i c_i \mathcal{P}^{0+}_{00} \Phi_{^6\mathrm{He}+2n^*}(\kappa;\lambda, d_\lambda, b_\lambda = b_\alpha) \\ &+ \sum_j c_j \mathcal{P}^{0+}_{00} \Phi_{\mathrm{DC}}(\lambda, d_\lambda, b_\lambda;\beta, b_n).\end{aligned} \tag{3}$$

Here, $\mathcal{P}^{0+}_{00}$ denotes the projection operator; κ assigns the neutron configuration in the ^{6}He core; $i = \{\lambda, d_\lambda\}_i$ and $j = \{\lambda, d_\lambda, b_\lambda;\beta, b_n\}_j$ are the selected computational values for the generator coordinates corresponding to the dissociation strength of the $2n^*$ cluster (λ), distance between the ^{6}He core and $2n^*$ cluster (d_λ); size of the $2n^*$ cluster (b_λ), volume for the ^{2}n-pair movement (β); and size of the ^{2}n-pair (b_n). The weight coefficients $c_{i,j}$ are determined by the diagonalization of the Hamiltonian. The characteristics of these 0^+ states can be analyzed via their overlap with the well-formed dineutron condensation w.f. Φ_{DC}:

$$\begin{aligned}&\mathcal{N}^{^8\mathrm{He}}_{\mathrm{DC}}(\beta, b_n) \\ &= |\langle \mathcal{P}^{0+}_{00} \Phi_{\mathrm{DC}}(\lambda = \lambda_0, d_\lambda = d_0, b_\lambda = b_\alpha;\beta, b_n) | \Psi_{^8\mathrm{He}(0^+)} \rangle|^2.\end{aligned} \tag{4}$$

This overlap is equivalent to the projection of the eigenstate w.f. onto the RGM clustering basis. The BEC character of the ^{8}He(0^+_2) state obtained from this RGM + GCM calculation is displayed in Fig. 2. This work demonstrates the flexibility and powerful ability of using the RGM combined with the GCM.

Notably, when extending the inter-cluster coordinate to a large range, the GCM can be applied to scattering problems. The first treatment of the scattering problem using GCM was reported in 1970 by Horiuchi [71]. Since then, significant progress has been achieved in this direction [15, 72–75].

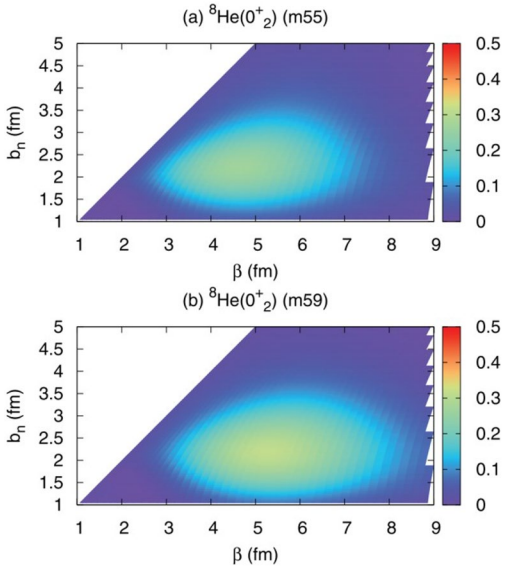

Fig. 2 (Color online) The overlaps of the ^{8}He(0^+_2) state with the dineutron-condensation w.f. on the β-b_n plane. **a**, **b** Results of the m55 and m59 interaction parameter sets, respectively. These parameter sets have different Majorana, Bartlett, and Heisenberg parameter values in the central force. The figures are taken from Ref. [59]

2.3 Orthogonality condition method

The calculations in the RGM + GCM approach can be simplified further using the orthogonality condition method (OCM), which was initially proposed by Saito in 1968 [14]. The idea is to exclude the states for the relative motion of the clusters that are occupied by the internal structure of the clusters themselves, namely $\langle\varphi_i|\chi(\boldsymbol{r})\rangle = 0$ for φ_i, representing the internal states of the clusters, and $\chi(\boldsymbol{r})$, which is the between-cluster relative motion w.f.. The detailed formulation of the OCM can be found in Ref. [67].

OCM was proven to be highly effective in describing the complex nuclear cluster structure and scattering. In the 1970s, Matsuse and Kamimura conducted quantitative computations using OCM and indicated that the first $K^\pi = 0^-$ band of ^{20}Ne exhibits a strong α-clustering character, whereas the ground state band predominantly displays shell-model-like structures [76]. Notably, Horiuchi extended the OCM to address the multi-cluster problems and reproduced the binding energy and excited levels of ^{12}C, thus revealing the coexistence of the shell model-like and molecular-like structures [77]. In recent years, OCM has been applied to the structure of the ^{13}C nucleus to investigate the influence of the additional valence neutron upon the 3α core [78–80]. Moreover, Yamada has extended the OCM calculations to a large multi-cluster model space and revealed that the 0^+_6 state of ^{16}O, which is approximately 2 MeV above the 4α breakup threshold, exhibits a significant 4α-condensation character. Similar work was also conducted for the $2\alpha + t$ configuration in ^{11}B [81].

2.4 Molecular orbit model and generalized two-center cluster model

The molecular viewpoint of nuclear structure was introduced by Wheeler in 1937 [82], the same year the release of the RGM [12]. This is natural, as the interactions between groups (clusters) are quite similar to molecular bonds in atomic physics. The molecular picture supports the excessive binding energy of the α-conjugate nuclei, which is roughly proportional to the number of bonds between α-particles [11]. This concept was further developed and applied to light nuclei to account for the energy-level spectra, which could be classified into the molecular rotational bands together with the proposal of the "threshold rule (Ikeda diagram)" [21, 23, 83, 84].

The MO model was proposed for nuclei with excessive nucleons in addition to cluster cores, particularly unstable neutron-rich or proton-rich nuclei [3, 29, 30, 39, 85, 86]. The basic idea is to exploit the multicenter potential, corresponding to the cluster cores, within which the valence nucleons move around one core or multiple cores, similar to the valence electrons playing roles in ionic or covalent bonding between atoms, respectively. The MO states may occur at energies below the cluster-separation threshold and create bound (lower-lying) molecular structures [3, 86]. Here, we illustrate a simple case of a two-center system, such as that for ^{9,10}Be. The molecular w.f. can be formed by the linear combination of nuclear orbitals (LCNO):

$$\Phi^{K,\Pi}_{\mathrm{LCNO}}(\boldsymbol{R},\boldsymbol{r}_n) = N(R)\frac{1}{\sqrt{(1+\delta^{K,p}(\boldsymbol{R}))}} \times \left[C_1\Psi_{\alpha_1}\Psi_{\alpha_2}\Phi^K_{n,l_1}(\boldsymbol{r}_{n\alpha_1}) + (-1)^p C_2\Psi_{\alpha_1}\Psi_{\alpha_2}\Phi^K_{n,l_2}(\boldsymbol{r}_{n\alpha_2})\right], \tag{5}$$

where $\boldsymbol{R}$ is the vector connecting the c.m. of the two α cores, $\boldsymbol{r_n}$ is the vector between the c.m. of the 2α system and the valence neutron, $\boldsymbol{r}_{n,\alpha i}$ the vector between the c.m. of each α core and the valence neutron (Fig. 13 described in Ref. [3]), $\Psi_{\alpha i}$ is the internal w.f. of each α core, $\Phi^K_{n,li}$ the single-particle w.f for the valence neutron around each core (^{5}He state) with an l_i orbital angular momentum of and K projection of its total angular momentum onto the direction of $\boldsymbol{R}$, and $\delta^{K,p}$ is the nonorthogonality factor determined by the overlap of the two single-particle w.f.s associated with α_1 and α_2. The phase $(-1)^p$ defines the gerade (g, positive sign) and ungerade (u, negative sign) properties, which give rise to the parity of the entire molecular system $\Pi = (-1)^{p+l}$. In addition, C_i gives the amplitudes for the sharing of valence neutrons between the two α-centers, with an extreme case of ionic bonding for $C_1 = 1$ and $C_2 = 0$, and vice versa. Neglecting the effect of the spin of the valence neutron, K becomes m, which represents the projection of l_i (=1 in the case of ^{9,10}Be) onto the symmetry axis. A value of $m = 0$ would yield a π-bond configuration, corresponding to the valence neutron mostly distributed outside the symmetry axis, whereas $m = 1$ would yield a π-bond configuration for the valence neutron distributed mainly along the symmetry axis, as depicted in Fig. 3. By taking the distance between the 2α core as a generator coordinate and by using more l_i shell orbitals, the molecular states can be calculated as shown in Fig. 4.

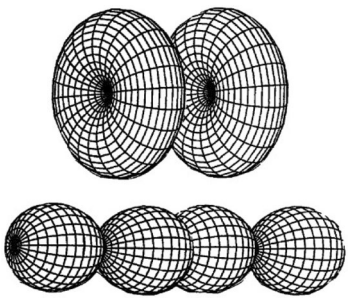

Fig. 3 (Color online) Illustration of the spacial overlap of two ^{5}He($p_{3/2}$) orbits corresponding to m for π-bond (upper part) and m for σ-bond (lower part) molecular orbitals, respectively. This figure was taken from Ref. [3]

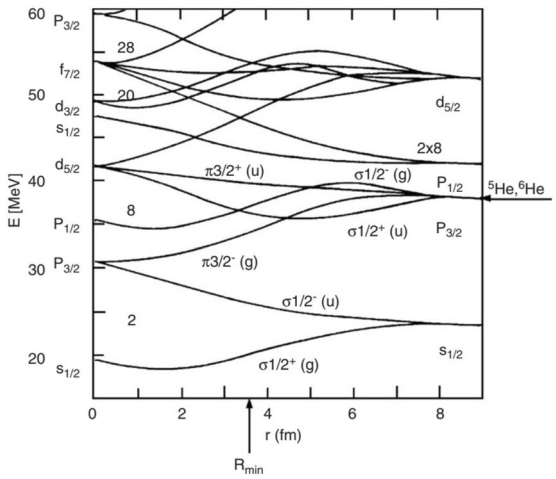

Fig. 4 (Color online) Molecular orbitals for a two-center system. At $R_{\rm min}$, the α–α–n potential attains its minimum. The quantum numbers (K, parity, and gerade and ungerade (g and u) properties) for various two-center orbits are indicated. The orbitals become ionic at large values of R. This figure was taken from Ref. [3]

Okabe and Abe reproduced the properties of the low-lying levels of ^{9}Be [29, 30] using the MO model. Itagaki et al. predicted the exotic behaviors in excited states of ^{16}C in which two neutrons occupy a σ orbit while another two neutrons occupy a π orbit, thus offering new insights into neutron-rich carbon isotopes [87].

Since the MO model is limited in its descriptions of the low-lying states of light neutron-rich nuclei, an extended molecular-type model, namely, the GTCM, was introduced by Ito et al. [40, 88, 89]. This method combines the covalent configuration, similar to the LCNO, with the ionic configuration and solves the equation of state as a function of the distance between the two centers (which is used as a generator coordinate) in a unified way. The model can then be applied to predict highly excited resonant states in which the two correlated centers may become two quasi-independent clusters, with each valence particle being combined into one as an ionic system. These resonant states then undergo decays, according to the cluster partial widths. Taking ^{12}Be ($\alpha + \alpha + 4$n) as an example, the basis function within the GTCM approach can be expressed in the form [40, 89]:

$$\Phi^{J^\pi K}_{\boldsymbol{m}}(S) = \mathcal{P}^{J^\pi}_{K}\,\mathcal{A}\left\{\psi_{\rm L}(\alpha)\psi_{\rm R}(\alpha)\prod_{j=1}^{4}\varphi_j(m_j)\right\}_S \tag{6}$$

with $\mathcal{A}$ representing the antisymmetrization operator for all nucleons, $\mathcal{P}^{J^\pi}_{K}$ being the projection onto the eigenstate with a total spin of J, projection of K, and total parity of π. The relative distance parameter between the 2α centers is S, which is variational as a generator coordinate. The w.f. for the α core, denoted by $\psi_i(\alpha)$ (i = L or R), has a $(0s)^4$ configuration of its harmonic oscillator centered at the left (L) or right (R) cluster. The shell-like single-particle w.f. is described by $\varphi_j(m_j)$ (j = 1 to 4). The symbol $\boldsymbol{m}$ represents the set $\{m_1, m_2, m_3, m_4\}$, where each m_j term represents a set of indices for a shell-like orbit $\{l_j, i_j, \tau_j\}$ with an orbital angular momentum of l_j, associated center of i_j (L or R), and spin projection of τ_j ($\uparrow$ or $\downarrow$).

The total w.f. is obtained by taking a superposition over S, $\boldsymbol{m}$, and K as:

$$\Phi^{J^\pi} = \int {\rm d}S \sum_{\boldsymbol{m},K} C_{\boldsymbol{m}K}(S)\Phi^{J^\pi K}_{\boldsymbol{m}}(S), \tag{7}$$

The summation includes all covalent and ionic configurations because of all the combinations of i_j (L or R). The amplitude $C_{\boldsymbol{m}K}(S)$ can be determined by solving the coupled channel GCM equation:

$$0 = \int {\rm d}S \sum_{\boldsymbol{m}K} C_{\boldsymbol{m}K}(S)\langle\Phi^{J^\pi K'}_{\boldsymbol{m}'}(S')|H - E^{J^\pi}|\Phi^{J^\pi K}_{\boldsymbol{m}}(S)\rangle. \tag{8}$$

GTCM naturally captures the formation of covalent molecular orbits as well as the ionic cluster states, depending on the relative distance S. Figure 5 shows the GTCM predicted $J^\pi = 0^+$ states in ^{12}Be [90]. The low lying states are basically dominated by the covalent configurations, whereas the higher lying states are closer to the ionic configurations because of the expansion of the system size (larger

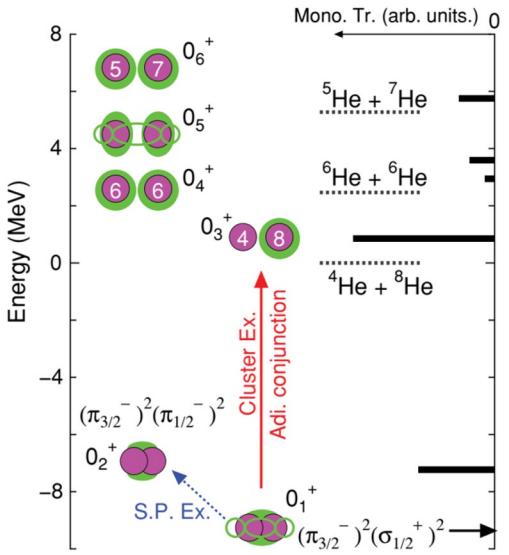

Fig. 5 (Color online) The intrinsic structures and energy positions for the 0^+ excited states of ^{12}Be are shown by the illustrations on the left side, whereas the histograms on the right show the respective monopole transition strengths. The horizontal dashed lines show the indicated cluster-separation thresholds. The bottom-right arrow represents the energy position of the ground state. The blue-dashed arrow represents the single-particle excitation, whereas the red-solid arrow indicates the cluster excitation in adiabatic conjunction form. This figure was taken from Ref. [90]

S). Particularly, the predicted 0_3^+ state, configured as ^{4}He + ^{8}He, has a large monopole transition strength from the g.s., which is an observable imprint of the cluster-structure formation in a 0^+ state with a relatively low excitation energy [90]. This prediction has been confirmed by the following experiment [46].

2.5 Antisymmetrized molecular dynamics and fermion molecular dynamics

In the 1960s, the Brink w.f. was proposed to describe the nuclear structure using the wave-packet concept rather than the orbit configurations [22]. Basically, each nucleon or a group of nucleons is presented by a Gaussian function centered at a position $\boldsymbol{R}$. Many $\boldsymbol{R}$s values can become the generator coordinates, and various wave-packet configurations can be combined and fixed, according to the weights determined by the GCM equation. The wave-packet basis is in favor of describing the clustering system within a limited state space, whereas the orbit configurations are better suited to account for the single-particle behaviors in a centralized mean field. Brink-type w.f.s have since been accepted and extended by many cluster-oriented models, such as AMD and THSR [25, 32].

In the AMD model, each nucleon is described by a Gaussian wave packet, which can be regarded as the extreme of the Brink w.f.. The model originated from the quantum molecular dynamics (QMD) approach used to simulate the heavy-ion reactions, but was implemented by applying the full antisymmetrization among all nucleons to account for the real nuclear structure [32, 33, 91]. FMD is similar to AMD, but FMD incorporates a variable width parameter for the Gaussian-type wave packet [92]. Both AMD and FMD consistently suggest that the second 0^+ state of ^{12}C (the Hoyle state) has a prominent gas-like 3α configuration with an extended size [92–94].

The AMD w.f. for a nucleus is expressed as a Slater determinant composed of single-nucleon Gaussian wave functions:

$$\Phi_{\mathrm{AMD}}(\mathbf{Z}) = \frac{1}{\sqrt{A!}}\mathcal{A}\{\varphi_1, \varphi_2, \ldots, \varphi_A\}, \tag{9}$$

where $1/\sqrt{A!}$ is a normalization factor and φ_i describes the single-particle w.f. of the ith nucleon, which is a product of a spatial part ($\phi_{\mathbf{Z}_i}$), an intrinsic spin part (χ_i), and an isospin part (τ_i):

$$\varphi_i = \phi_{\mathbf{Z}_i} \cdot \chi_i \cdot \tau_i. \tag{10}$$

The spatial wave function, denoted by $\phi_{\mathbf{Z}_i}$, is given by:

$$\phi_{\mathbf{Z}_i}(\boldsymbol{r}_j) = \left(\frac{2\nu}{\pi}\right)^{4/3} \exp\left\{-\nu\left(\boldsymbol{r}_j - \frac{\boldsymbol{Z}_i}{\sqrt{\nu}}\right)^2\right\}, \tag{11}$$

where $\boldsymbol{Z}_i$ presents the center of the Gaussian wave packet. The size parameter ν is common to all nucleons. The intrinsic spin can be expressed in the form:

$$\chi_i = \left(\frac{1}{2} + \xi_i\right)\chi_\uparrow + \left(\frac{1}{2} - \xi_i\right)\chi_\downarrow, \tag{12}$$

where the ξ_i parameter provides the specific gravity of components with different spin orientations. If all the Gaussian functions in the AMD w.f. (Eq. 11) are centered around a common position, the resulting w.f. resembles a shell-model-like w.f.. These results indicate a distribution of nucleons with individual wave packets localized around a single center. However, if the Gaussian functions are centered around multiple positions, the AMD w.f. gives rise to a multi-cluster structure that is equivalent to the Brink w.f..

The Hamiltonian of the AMD can be given by:

$$\hat{H} = \sum_{i=1}^{A}\frac{\hat{p}_i^2}{2m_i} + \sum_{i<j}V_{ij}^{(2)} + \sum_{i<j<k}V_{ijk}^{(3)} - T_{\mathrm{c.m.}}, \tag{13}$$

where A denotes the total number of nucleons, $T_{\mathrm{c.m.}}$ denotes the center-of-mass kinetic energy, and $V_{i,j}^{(2)}$ and $V_{i,j,k}^{(3)}$ denote the two-body and three-body interactions, respectively. The two-body part can be specified as:

$$\begin{aligned} V_N^{(2)} &= \left(\omega + b\hat{P}_\delta + h\hat{P}_\tau - m\hat{P}_{\delta\tau}\right)\left[V_{\mathrm{A}}e^{-\frac{r_{ij}}{a_{\mathrm{A}}}} + V_{\mathrm{R}}e^{-\frac{r_{ij}}{a_{\mathrm{R}}}}\right], \\ V_{LS}^{(2)} &= \left(U_{\mathrm{A}}e^{-\frac{r_{ij}}{a_{\mathrm{A}}}} + U_{\mathrm{R}}e^{-\frac{r_{ij}}{a_{\mathrm{R}}}}\right)\hat{P}(^3O)\hat{L}\cdot\left(\hat{S}_i + \hat{S}_j\right), \\ V_{ijk}^{(2)} &= v_3(\boldsymbol{r}_i - \boldsymbol{r}_j)\delta(\boldsymbol{r}_i - \boldsymbol{r}_k). \end{aligned} \tag{14}$$

where V_N^2 is the nucleon-nucleon interaction, V_{LS}^2 the coupling term for intrinsic orbits, $\hat{P}_\sigma$ is the spin exchange operator, and $\hat{P}_\tau$ the isospin exchange operator. The subscripts A and R correspond to the attractive and repulsive interactions, respectively. Last, $\hat{P}(^3O)$ is the projection operator. The two-body interaction parameters are usually taken from the Volkov, Minnesota, parameter sets [95, 96] or the widely used Gogny forces. Here, V_{ijk}^3 represents the density-dependent three-body force, and v_3 indicates its strength. Strong correlations between nucleons within the cluster structure emphasize the significance of multi-body correlations in understanding the clustering structure. The energy of the system can then be calculated according to:

$$E = \frac{\langle\Phi_{\mathrm{AMD}}|H|\Phi_{\mathrm{AMD}}\rangle}{\langle\Phi_{\mathrm{AMD}}|\Phi_{\mathrm{AMD}}\rangle}. \tag{15}$$

The positions of wave packets vary under the influence of nuclear forces until they reach a stable configuration that corresponds to the minimum energy state of the system. However, at this stage, the w.f. obtained using Eq. 9 does not satisfy the requirements of parity or angular momentum symmetry. To restore their symmetry, it is necessary to obtain the eigenwave functions of spin and angular momentum via spin parity projection:

$$\begin{aligned}\Phi^{\pm}(\mathbf{Z}) &= \mathcal{P}^{\pm}\Phi_{\mathrm{AMD}}(\mathbf{Z}) = \frac{1\pm\mathcal{P}_r}{2}\Phi_{\mathrm{AMD}}(\mathbf{Z}),\\ \Phi^{J\pm}_{MK}(\mathbf{Z}) &= \mathcal{P}^{J}_{MK}\Phi^{\pm}(\mathbf{Z}) = \int \mathrm{d}\Omega D^{J*}_{MK}(\Omega)\mathcal{R}(\Omega)\Phi^{\pm}(\mathbf{Z}),\end{aligned} \tag{16}$$

where $\mathcal{P}^{\pm} = (1\pm\mathcal{P}_r)/2$ and $\mathcal{P}^{J}_{MK} \equiv \int \mathrm{d}\Omega D^{J*}_{MK}(\Omega)\mathcal{R}(\Omega)$ are the parity projection and total angular momentum projection operators, respectively; Ω denotes the solid angle; $\mathcal{R}(\Omega)$ denotes the rotation operator; and $D^{J*}_{MK}(\Omega)$ the standard Wigner's D function. The K number for each spin parity is determined based on the principle that the energy expectation value for the spin parity eigenstate $\Phi^{J\pm}_{MK}(\mathbf{Z})$ is minimized [94]. Moreover, the AMD basis w.f. starts with a random initial distribution of nucleons. Many such bases must be superposed to produce various eigenstates of the nucleus, in a way similar to the application of GCM [33].

Over the past thirty year, AMD has been developed to provide not only the energy eigenvalues and nuclear radii but also other observables, such as the cluster decay widths, magnetic dipole and electric quadrupole moments, and electromagnetic transition probabilities. Recently, AMD has successfully reproduced experimental properties of various nuclei, including Be, C, O, and Ne isotopes [33], and it has become a powerful tool for investigating the cluster and molecular structures in atomic nuclei [17]. Here, we illustrate typical examples that are closely related to the latest experimental findings.

In 1998, Kanada-En'yo used the AMD model to reproduce all energy levels below 15 MeV in ^{12}C together with the related $E2$ transition rates and β-decay strengths [97]. Subsequently, the AMD model was extended to investigate the excited states of ^{10}Be using the variation after projection technique [98]. Remarkably, without assuming preformed 2α clusters, AMD calculations unveiled a notable $2\alpha + 2$n cluster structure in many intrinsic states of ^{10}Be [98]. To extract the behaviors of the valence nucleons, the single-particle Hamiltonian under the AMD framework can be defined in the following form [99]:

$$\begin{aligned}h_{\alpha\beta} = \langle\tilde{\varphi}_\alpha|\hat{t}|\tilde{\varphi}_\beta\rangle + \sum_{\gamma=1}^{A}\langle\tilde{\varphi}_\alpha\tilde{\varphi}_\gamma|\hat{v}^N + \hat{v}^C|\tilde{\varphi}_\beta\tilde{\varphi}_\gamma - \tilde{\varphi}_\gamma\tilde{\varphi}_\beta\rangle\\ + \frac{1}{2}\sum_{\gamma,\delta=1}^{A}\langle\tilde{\varphi}_\gamma\tilde{\varphi}_\delta|\tilde{\varphi}^*_\alpha\tilde{\varphi}_\beta\frac{\delta\hat{v}^N}{\delta\rho}|\tilde{\varphi}_\gamma\tilde{\varphi}_\delta - \tilde{\varphi}_\delta\tilde{\varphi}_\gamma\rangle.\end{aligned} \tag{17}$$

The single-particle orbits can be expressed as $\tilde{\phi}_s = \sum_{\alpha=1}^{A} f_{\alpha s}\tilde{\varphi}_\alpha$, where $f_{\alpha s}$ represents the eigenvectors of $h_{\alpha\beta}$. Within this framework [39, 98], the two valence neutrons in ^{10}Be occupy molecular orbits around the 2α clusters with band heads of $K^\pi = 0^+, 1^-, 0^+_2$, corresponding to the two valence neutrons occupying the π^2, $\sigma\pi$, and σ^2 bonds, respectively.

Later, Baba et al. extended the AMD calculation to ^{16}C, ^{14}C, and ^{14}O nuclei [65, 66, 100, 101]. They identified 3-cluster structures with various valence-neutron configurations, as shown in Fig. 6. Panels (a) and (b) show the ground-state rotational bands of ^{16}C [66], which exhibit approximately spherical structures. Panels (c) and (d) display asymmetric triangular rotational band structures, with 0^+_2 and 2^+_5 as the band head members, respectively. Panels (e) and (f) depict linear chain structures with a $(3/2^-_\pi)^2(1/2^-_\sigma)^2$ configuration. The reversed moment of inertia for this band is $\frac{\hbar^2}{2\mathcal{I}} \sim 112$ keV, which agrees with the experimental result of $\frac{\hbar^2}{2\mathcal{I}} \sim 122$ keV reported by Liu et al. [49]. Figure 7 shows the functional relationship between the positive parity energy levels and the quadrupole deformation parameter β [101]. The black circles, triangles, and squares represent the structures of the ground state, triangular, and $(3/2^-_\pi)^2(1/2^-_\sigma)^2$ linear chain rotational bands, respectively. In addition, in the higher excitation energy region near $\beta = 1.6$, a peculiar linear chain structure with a pure σ configuration may exist [101], namely $(1/2^-_\sigma)^2(1/2^+_\sigma)^2$. The energy of the band-head is $E_x \doteq 31.72$ MeV (0^+) with a reversed moment of inertia

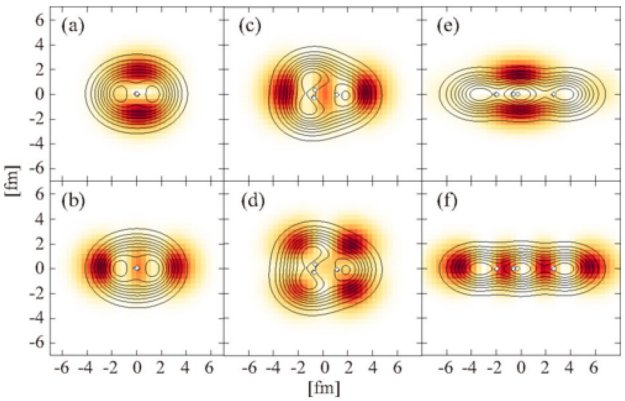

Fig. 6 (Color online) Density distributions of the AMD-predicted positive-parity states in ^{16}C, with **a**, **b** ground, **c**, **d** triangular, and **e**, **f** linear chain configurations. The contour lines show the proton density distributions. The color plots display the single-particle orbits occupied by four valence neutrons. The lower panels show the two most weakly bound neutrons, whereas the upper panels show the other two valence neutrons. Open boxes show the centers of the proton wave packets. This figure was taken from Ref. [66]

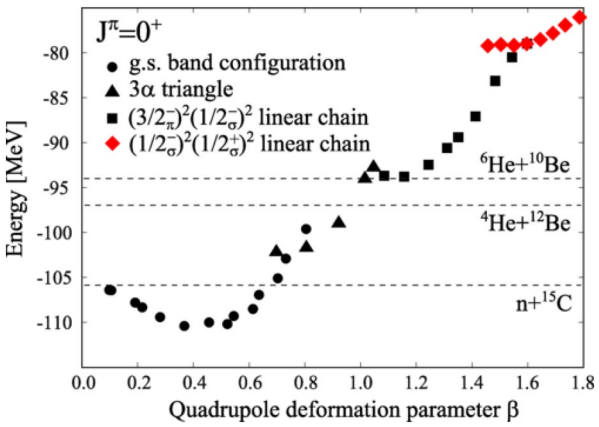

Fig. 7 (Color online) Calculated energy curves ($J^\pi = 0^+$) as a function of the quadrupole deformation parameter β for ^{16}C. Four different cluster structures are marked by circles, triangles, squares, and diamonds. The corresponding threshold energies are shown by dashed lines. This figure is taken from Ref. [101]

$\frac{\hbar^2}{2\mathcal{I}}$ of ~ 50 keV, which is significantly smaller than that of the $(3/2^-_\pi)^2(1/2^-_\sigma)^2$ configuration [101]. This state was suggested in Ref. [49] to correspond with the tentatively observed 27.2 MeV state.

Various exotic clustering configurations have been predicted [65, 99, 100] and observed [102, 103] for ^{14}C, including triangular, π-bond, and σ-bond linear chain structures. Baba et al. analyzed the associated decay patterns. Their results indicated that the σ-bond linear chain structure primarily decays into the ~ 6 MeV states of ^{10}Be, whereas other resonant states mainly decay into the ground and first excited states (3.4 MeV, 2^+), as illustrated in Fig. 8. These selective decay paths provide an important means by which to identify the existence of the σ-bond linear chain configuration, which was effectively used in later experiments conducted by Li et al. [48] and Han et al. [50].

A theoretical comparison was made between the mirror nuclei ^{14}C and ^{14}O, regarding their molecular structures [100]. Figure 9 shows the excitation energies of the 0^+ states in ^{14}C and ^{14}O, corresponding to the ground, triangle, and linear chain configurations. The shift between a pair of states, mostly caused by Coulomb interactions, also known as the Thomas–Ehrman Shift (TES) [104–106], is related to the expansion (in terms of size and deformation) of the corresponding systems. The measurement of the TES for ^{14}C and ^{14}O, in comparison to the calculated values, would provide new evidence for the existence of the intriguing linear chain structure in exotic nuclei.

2.6 THSR wave function and container model

According to the Ikeda diagram [23], the α conjugate nuclei may be transformed into a multi-α clustering system at the vicinity of the corresponding separation energy. Owing to the small relative energy (decay energy) in this situation, the relative motion of these α-clusters could all be in s-wave. These results have stimulated the idea of α-condensation in nuclei, as proposed by Röpke et al. in 1998 [24]. Subsequently, the THSR w.f. was developed to investigate the 3α condensation in ^{12}C [25]. This w.f. can be regarded as a variant of the Brink w.f.. Whereas the Brink w.f. allows the subsystems (wave packets) to remain at random positions inside the nucleus, the THSR w.f. requires all subsystems

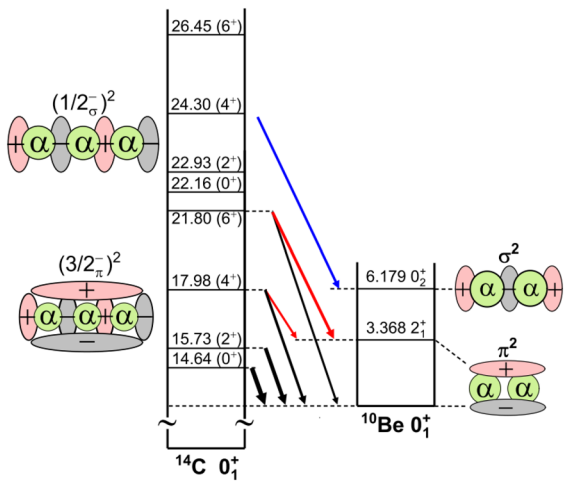

Fig. 8 (Color online) Schematic illustrating the selective decay pattern of the rotational band members of the π and σ linear chain structures in ^{14}C, as calculated by AMD [65, 99]

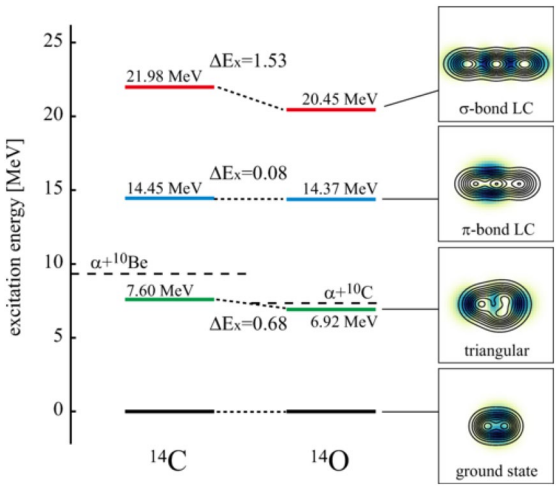

Fig. 9 (Color online) The comparison of excitation energies between the mirror-pair nuclei ^{14}C and ^{14}O for $J^\pi = 0^+$ states. The dashed lines represent theoretical thresholds. This figure was taken from Ref. [100]

(each with a spin of 0) to move in s-wave around the center of mass of the entire system [25], similar to the case of BEC [15, 17, 25, 26].

As an example, the THSR w.f. for a 3α system can be expressed as:

$$\Psi_{3\alpha}^{\mathrm{THSR}} = \mathcal{A}\left\{\exp\left[-\frac{2}{B^2}(\boldsymbol{X}_1^2+\boldsymbol{X}_1^2+\boldsymbol{X}_3^2+)\right]\Phi(3\alpha)\right\} = \exp\left(-\frac{\boldsymbol{\xi_3^2}}{B^2}\right)\mathcal{A}\left[\exp\left(-\frac{4\boldsymbol{\xi_1^2}}{3B^2}-\frac{\boldsymbol{\xi_2^2}}{B^2}\right)\Phi(3\alpha)\right], \tag{18}$$

where $\mathcal{A}$ is the antisymmetrization operator, B is a parameter characterizing the overall size of the nucleus, $\boldsymbol{X}_i$ is the c.m. of the ith α-cluster, and $\Phi(3\alpha) = \phi_{\alpha_1}\phi_{\alpha_3}\phi_{\alpha_3}$ is the 3α w.f.. The Jacobi coordinates $\boldsymbol{\xi}$ are related to $\boldsymbol{X}$ according to $\boldsymbol{\xi_1} = \boldsymbol{X}_1 - 1/2(\boldsymbol{X}_2 - \boldsymbol{X}_3)$, $\boldsymbol{\xi_2} = \boldsymbol{X_2} - \boldsymbol{X_3}$, and $\boldsymbol{\xi_3} = \frac{1}{3}(\boldsymbol{X_1} + \boldsymbol{X_2} + \boldsymbol{X_3})$. Equation 18 can be directly applied to the $^8\mathrm{Be}(0_1^+) + \alpha$ configuration, in which $\mathcal{A}\exp[\boldsymbol{\xi_2^2}/B^2]\phi_{\alpha_2}\phi_{\alpha_3}$ describes the $^8\mathrm{Be}(0_1^+)$ subsystem and $\exp[4\boldsymbol{\xi_1^2}/3B^2]\phi_{\alpha_1}$ represents the remaining α-particle [15, 17]. By utilizing the THSR w.f., the Hoyle state in ^{12}C can be accurately reproduced [25]. The THSR w.f. has also been utilized to investigate BEC-like structures in heavier nuclei, such as ^{16}O [15, 17, 25]. Moreover, the THSR w.f. has been extended to incorporate different size parameters B in different dimensions, thus enabling the description of nuclear deformations, including possible linear chain structures [15, 107].

The THSR w.f. has been widely adopted as a standard approach to evaluate the intrinsic components of BEC-like structures in any quantum state. For instance, the Hoyle state of ^{12}C obtained via the general RGM/GCM possesses an almost 100% overlap with an extended single THSR w.f. [15, 107, 108]

$$|\langle\phi(3\alpha\mathrm{RGM/GCM})|\phi(3\alpha\mathrm{THSR})\rangle|^2 \approx 100\%. \tag{19}$$

The inversion–doublet band (headed by $J^\pi = 0^+$ and $J^\pi = 0^-$ states) for the asymmetric $^{16}\mathrm{O} + \alpha$ structure in ^{20}Ne can also be described by a single THSR-type w.f. with different size parameters for the core ^{16}O and overall ^{20}Ne system [15, 109, 110]. These results imply that the THSR w.f. incorporating adjustable size parameters may represent some fundamental physical characteristics of the clustering states [15].

A container model based on the THSR w.f. was recently proposed [15, 38]. Unlike traditional cluster models, such as the Brink wave packet, the container model focuses on the dynamic evolution of containers to capture cluster motion. The container size evolves from smaller to larger values as the excitation energies increase. The cluster motion inside the mean-field potential is characterized by using the size parameter under the condition of full antisymmetrization among all nucleons. This approach has been studied and documented by Funaki et al. [15, 38]. The w.f., which is generally nonlocalized, can result in localized density distributions for clusters due to the Pauli blocking effect [15, 37]. With its relatively simple picture and parameter settings, the container model offers a relatively simple conceptual framework and parameter settings, thereby showing promise as a powerful alternative to traditional methods, such as the RGM and Brink-GCM, for describing cluster dynamics [15, 16]. As an example, Fig. 10 schematically illustrates the $\alpha + {}^8\mathrm{Be}$ cluster structure in ^{12}C and the $\alpha + {}^{12}\mathrm{C}$ cluster structure in ^{16}O under the "container" framework. In this model, 2α or 3α clusters are confined in a "container" characterized by the parameter β_1, while the remaining α cluster is confined in a larger "container" characterized by β_2 (where β_2 is related to the parameter B, as defined in Eq. 18).

In 2023, Zhou et al. reported the microscopic five-body calculations for ^{20}Ne [27], thus revealing a 0^+ state located approximately 3 MeV above the 5α threshold, which could correspond to the state observed in recent experiments [111]. This state exhibited the $^{16}\mathrm{O}\,(0_6^+) + \alpha$ structure, thereby indicating distinct characteristics of a 5α condensate state. The calculated partial α decay width from the 5α condensate state to the 4α condensate state was as high as 0.7 MeV due to the increased excitation energy. The monopole transition M(E0) between the condensate state and the ground state was ~ 1 fm^2. These characteristics are all similar to those of 3α and 4α condensate states.

2.7 α-cluster formation and decay from heavy nuclei

α clustering in heavy nuclei is essentially connected to α decay, which is generally described as the quantum tunneling of the preformed α particles via a semi-classical model initiated by George Gamow in the 1920s [9, 112, 113]. Various theoretical approaches have been developed to predict the half-life of α decay [114–125]. However, the preformation probability of the α-cluster within a heavy nucleus still cannot be reproduced from the shell-type calculations [126].

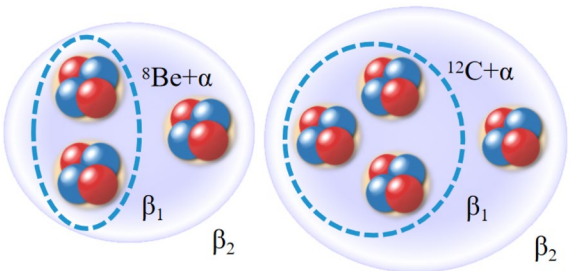

Fig. 10 (Color online) Schematic showing the $\alpha + {}^8\mathrm{Be}$ and $\alpha + {}^{12}\mathrm{C}$ systems within the "container" picture, in which multi-α (2α or 3α) and another α are in different "containers" characterized by the size parameters β_1 and β_2, respectively

These results are most likely attributable to the difficulties associated with accounting for the four-nucleon correlation in a complex multi-nucleon environment. Generally, this probability can only be obtained empirically by using the experimental decay probability and subtracting the calculated barrier penetrating factor [119, 127–130].

Recently, a novel microscopic approach for describing the α formation was proposed by Röpke et al. [131, 132] and developed by Xu et al. [124, 133]. The model aimed to create the quartetting w.f. (QWFA) for the four valence nucleons upon the remaining core of the nucleus. The introduction of the c.m. coordinates (new degree-of-freedom) for the quartet system (RGM–Brink-type) should have captured the main feature of the cluster-formation dynamics [121, 124, 131–134]. In QWFA, the w.f. of four valence nucleons is divided into two components [133]: the c.m. motion relative to the core and the intrinsic motion of the four nucleons relative to their c.m. [124]:

$$\Psi(\boldsymbol{R}, \boldsymbol{s}_j) = \varphi^{\text{intr}}(\boldsymbol{s}_j, \boldsymbol{R})\Phi^{\text{com}}(\boldsymbol{R}), \tag{20}$$

where $\boldsymbol{R}$ is the c.m. coordinate of the quartet and $\boldsymbol{s}_j = \boldsymbol{S}, \boldsymbol{s}, \boldsymbol{s}'$ are the Jacobi–Moshinsky coordinates for the quartet nucleons relative to $\boldsymbol{R}$ [121], as sketched in Fig. 11. The Hamiltonian for this quartet system contains the kinetic energy and the interaction potential which depends on both $\boldsymbol{R}$ and $\boldsymbol{s}_j$. The coupled equations can then be established for $\varphi^{\text{intr}}(\boldsymbol{s}_j, \boldsymbol{R})$ and $\Phi^{\text{com}}(\boldsymbol{R})$. The complex nonlocal interaction between the quartet and core can be approximately replaced by an effective local potential, which largely simplifies the calculation without changing the basic features of the potential.

Two different regions for $R < R_{\text{sep}}$ and $R > R_{\text{sep}}$ are considered to describe the α-decay process [121, 135, 136]. When $R < R_{\text{sep}}$, the intrinsic w.f. of the quartet represents four independent nucleons in quasi-particle states within the shell model framework. When $R > R_{\text{sep}}$, the nature of the intrinsic w.f. undergoes a transformation, signifying the emergence of a bound state that exhibits characteristics similar to those of an α-particle [119, 124]. Considering that the α-like state can only exist at densities lower than the critical value $\rho_c(R_c) = 0.02917\,\text{fm}^{-3}$ and dissolves at higher densities, the α-cluster preformation probability P_α can be calculated by integrating the bound-state w.f. $\Phi(r)$ from the critical radius R_c to infinity [121]:

$$P_\alpha = \int_{R_c}^{\infty} d^3R|\Phi(R)|^2\Theta[\rho_c - \rho_B(R)], \tag{21}$$

where $\rho_B(R)$ represents the baryon density at a distance of R from the core center. The probability of finding an α-particle at certain position R can be expressed as the square of the overlap between the quartet w.f. $\varphi^{\text{intr}}_{\text{quartet}}$ and free α-particle w.f. $\varphi^{\text{intr}}_{\alpha}$ (THSR-type), as exhibited in Fig. 12. Notably, the calculated α-cluster preformation factors and α-decay widths within the QWFA approach for a series of heavy nuclei are in good quantitative agreement with experimental observations (Fig. 2 of Ref. [133]). Hence, the QWFA can capture the main feature of the α-cluster preformation mechanism inside a heavy nucleus and thus provides a convincing means by which to solve a long-standing problem.

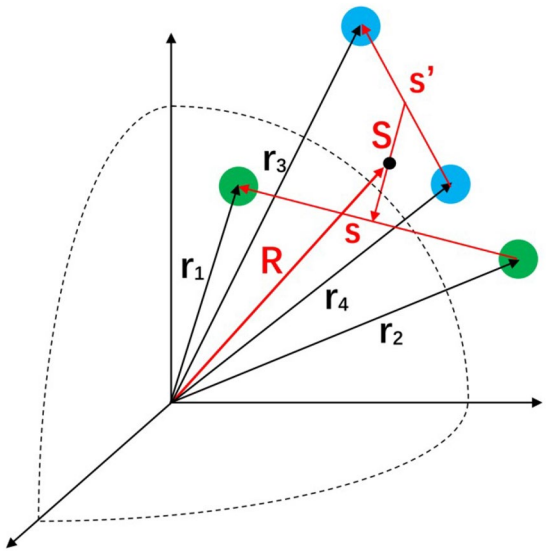

Fig. 11 (Color online) Sketch of quartet coordinates for two protons at positions $r_1 \uparrow$ and $r_2 \downarrow$ as well as two neutrons at $r_3 \uparrow$ and $r_4 \downarrow$. This figure was taken from Ref. [121]

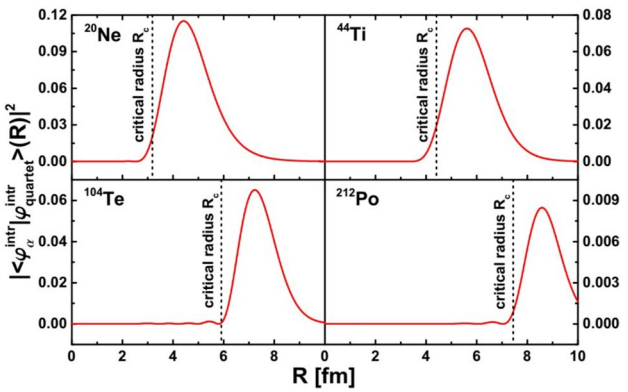

Fig. 12 (Color online) Overlaps between the intrinsic quartet and α -particle w.f.s as a function of R for the α + doubly magic core systems ^{20}Ne, ^{44}Ti, ^{104}Te, and ^{212}Po. This figure was taken from Ref. [121]

3 Experimental studies of nuclear clustering

Over the past thirty years, experimental studies of nuclear clustering have largely progressed along with the availability of radioactive ion beams(RIBs) for light, neutron-rich nuclei [4, 31, 49, 50, 60]. The experimental methods and techniques have also advanced to meet the requirements for clearly identifying nuclear clustering phenomena under the strong influence (mixing) of the shell-like effects. The experimental measurements generally started with the inclusive missing mass (MM) method in the early stages and gradually evolved into more and more exclusive methods incorporating various coincident detection techniques. The cluster decay and cluster knockout measurements are of special importance in the selective probing of the cluster structures from high-density single-particle states. These measurements, particularly those in inverse kinematics with the RIBs, normally require multi-particle detection in a small solid angle. Hence, the state-of-the-art position-sensitive (pixelated) detection systems have also advanced over the past two decades [28, 48–50].

3.1 Missing mass method and cluster production cross-sections

Experimental studies of cluster structure in light nuclei often start with inclusive measurements that typically require simple detection systems. The method relies on the assumption of a two-body system in both the initial and final channel of the reaction, i.e., $A(a, b)B$ or $a + A \rightarrow b + B$. With the properties of the beam (a) and target (A) particles being known and by measuring the energy and emission angle (position) of the projectile nucleus (b), the effective mass of the assumed recoil nucleus, denoted by m_{B^*}, can be deduced according to the conservation of energy and momentum in the reaction process. This process is equivalent to the deduction of the effective reaction Q-value described in the textbook [137]. The difference between this deduced effective mass (m_{B^*}) and its g.s. mass (m_B) is called the MM of the reaction, or the excitation energy of the nucleus B. Typical examples for the production of the excited states in ^{14}C can be found in Refs. [3, 138]. In these works, various reaction mechanisms are employed to populate the excited states in ^{14}C, including the two-neutron-transfer reactions ^{12}C(^{14}N, ^{12}N), ^{12}C(^{15}N, ^{13}N), and ^{12}C(^{16}O, ^{14}O), two-proton-transfer reaction ^{16}O(^{15}N, ^{17}F), and multi-nucleon-transfer reaction ^{9}Be(^{7}Li, d). The two-nucleon-transfer reactions are mostly in favor of populating the shell-like states, whereas the multi-nucleon transfer reaction can strongly populate the cluster-type states, owing to the associated multi-particle, multi-hole configurations. Different reaction Q-values, corresponding to different momentum mismatches, in the direct reactions may introduce different momentum transfers into the final particles which, in turn, may be placed into different spin-value ranges. Based on these carefully designed reaction tools and combined with theoretical model calculations, the shell-like states can be classified into various deformation schemes. The remaining states, particularly those that are significantly populated only in the multi-nucleon transfer reaction, could be grouped into cluster-based molecular rotational bands. Figure 13 shows the states in ^{14}C populated from the multi-nucleon-transfer reaction ^{9}Be(^{7}Li, d). The cluster-like states are grouped into two molecular rotational bands, corresponding to the parity-inversion-doublets [3, 138]. Notably, this double-band configuration at high excitation energies resulting from the reflection-asymmetric configuration, such as ^{10}Be + α in ^{14}C, constitutes strong evidence for the molecular (cluster) structure formation in atomic nuclei [21]. The energy gap between the two bands can be estimated according to the asymmetric structure

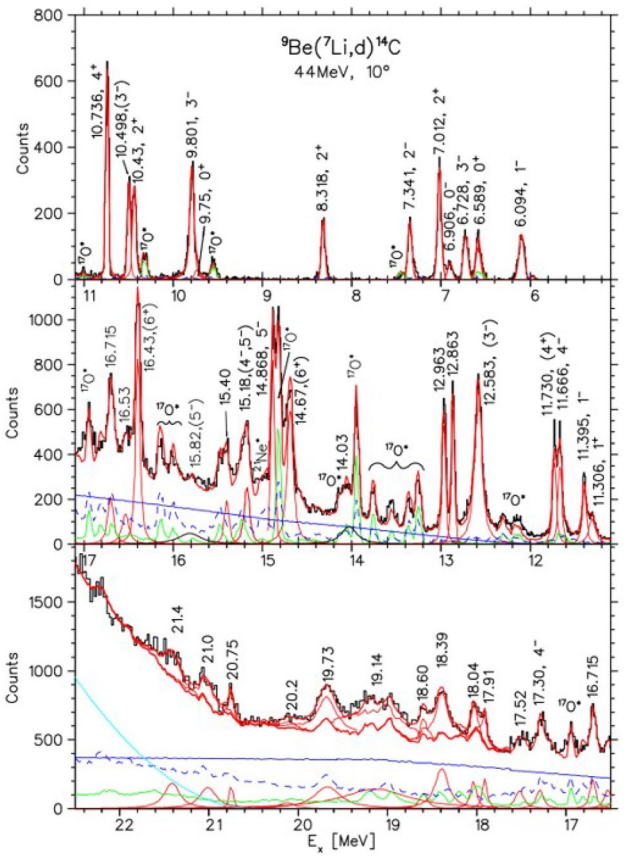

Fig. 13 (Color online) Deuterium spectrum from the multi-nucleon-transfer reaction ^{9}Be(^{7}Li, d). The structured backgrounds shown are three- and four-body continua or measured backgrounds with ^{12}C and ^{16}O targets, as depicted by the full and dashed lines and indicated as ^{17}O* and ^{21}Ne*, respectively. This figure was taken from Refs. [3, 138]

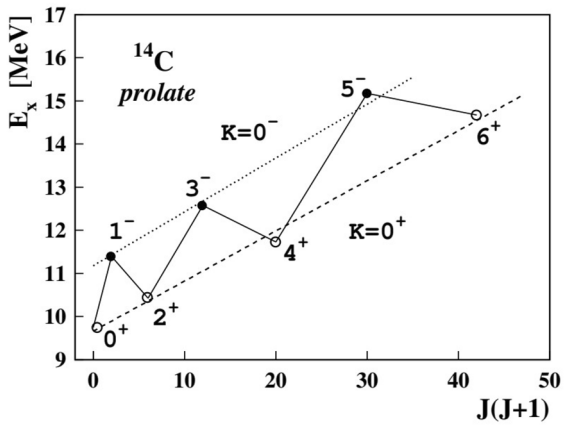

Fig. 14 (Color online) Proposed prolate-type α-cluster bands in ^{14}C. These are states that cannot be attributed to single-particle states. Their energies are plotted as a function of their assumed spins, $J(J+1)$, forming the parity-inversion-doublet rotational bands related to the reflection-asymmetric configuration, such as ^{10}Be + α in ^{14}C. This figure was taken from Ref. [138]

configuration. Similar exemplars for the study of cluster structures in nuclei via inclusive MM measurement can also be found in works such as Ref. [139] for ^{20}O (see Fig. 14).

The inclusive measurements may also incorporate the experimental determination of the cluster production cross-section in various reaction processes. An early typical study of this kind was reported in Ref. [140], where the He-cluster breakup and neutron removal cross-sections for $^{10-12,14}$Be were reported. It is interesting to see the persistence of the He-cluster structure within the neutron-rich Be isotopes up to the dripline nucleus ^{14}Be, as was demonstrated by comparing the measured He-cluster breakup cross-section with the phase-space estimation. In an inverse kinematics experiment, using A and a to denote the projectile and the target, respectively, the aforementioned MM measurement of the recoil nucleus b can be combined with the selected cluster production related to the breakup of the nucleus B in order to probe the cluster production cross-section as a function of the excitation energy. A representative example can be found in Ref. [141], in which the MM measurement of the triton particle from the ^{19}F(^{3}He,t)^{19}Ne reaction was made in coincidence with the proton or α decayed from the possible resonant states of ^{19}Ne. As such, the α-cluster production is observed as a function of the ^{19}Ne-excitation energies. This provides crucial information about the cluster-formation probability along the excitation axis, comprising both direct breakup and resonance-decay two-step processes, as depicted in Fig. 15.

3.2 Invariant mass method

The invariant mass (IM) method is dedicated to the resonant states, often at higher excitation energies that decay into fragments. As described above, the MM measurement is inclusive and sensitive to all kinds of states characterized by such as single-particle motion, collective motion, and cluster structures. Particularly, at high excitation energies the spectrum is generally dominated by a continuum associated with a high-level density. To improve the sensitivity to the clustering states and avoid as much of the overwhelmingly strong continuum background as possible, it is essential to measure the cluster-decay process [49]. The latter can be used to reconstruct the excitation energy of the reaction-produced cluster-like mother nucleus via the IM method, to

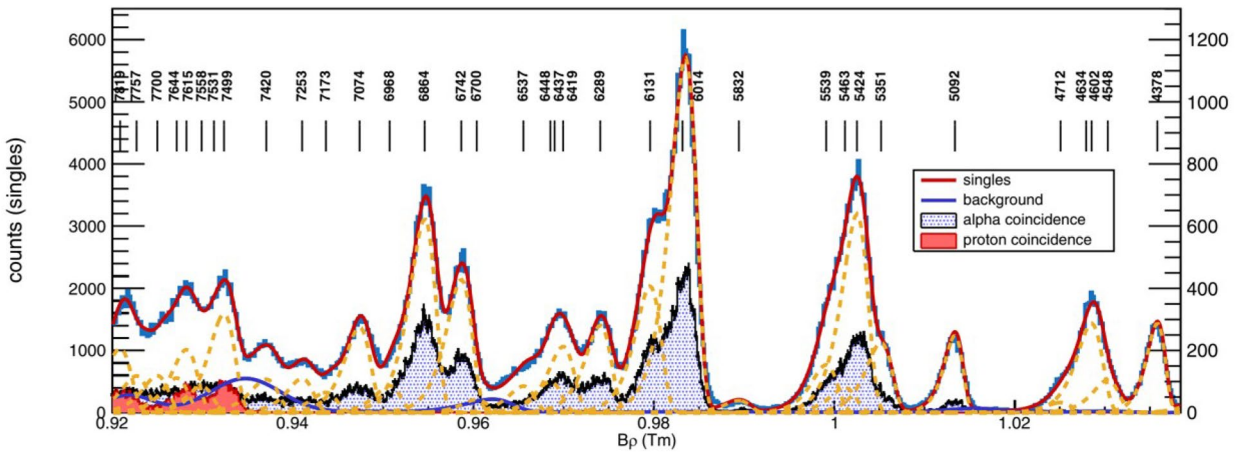

Fig. 15 (Color online) Triton spectrum measured from the ^{19}F(^{3}He,t) reaction with a beam energy of 25 MeV [141]. Events with α-particle detection (blue) or proton detection (red) in coincidence are also shown. The result of the fit function is shown in red, and individual peaks are highlighted in yellow. The background originating from the (^{3}He, d) reaction has been shown in blue. This figure was taken from Ref. [141]

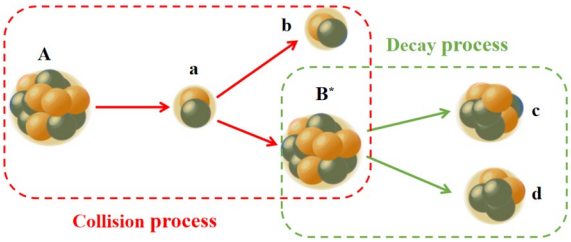

Fig. 16 (Color online) The schematic of the reaction $a(A, B^* \longrightarrow c + d)b$. The two-body collision process is presented in the red-line box, whereas the cluster-decay of a resonant state is displayed in the green-line box

determine the spins of the resonances based on the model-independent angular correlation analysis, extract the spectroscopic factor of the cluster structure in an observed resonant state, deduce the strength of a typical cluster excitation mode (e.g. the monopole-transition strength), and connect the unknown structures of the mother nucleus to the known structures of the detected daughter fragments via selective decay paths [46, 49, 50, 142]. Here, we highlight some useful quantities for the measurements and data analyses.

3.2.1 Kinematics

The IM method lies in a two-step process, namely, the resonance excitation followed by the cluster decay, as expressed by $a(A, B^* \rightarrow c + d)b$ in inverse kinematics and depicted in Fig. 16. Using relativistic expressions, the sum of the squares of the four-dimensional momentum (P^μ) is a Lorentz invariant quantity in different inertial reference frames. For a resonance-decay process, the IM method can be expressed as:

$$P^\mu P_\mu = \left(\frac{E}{c}, \boldsymbol{p}\right) = \frac{E^2}{c^2} - \boldsymbol{p}\cdot\boldsymbol{p} = m_{B^*}^2 c^2, \tag{22}$$

where m_{B^*} represents the total mass of the mother nucleus (resonance) B^*, $m_{B^*}^2 c^2$ is the square of the four-dimensional momentum in the c.m. system, $E = \sum_i E_i$ and $\boldsymbol{p} = \sum_i \boldsymbol{p}_i$ are the sums of the total energy and total three-dimensional momentum, respectively, of all the decay fragments in the laboratory system. The values of E_i and $\boldsymbol{p}_i$ can be deduced from experimental measurements.

The relative energy of the decay system, such as that shown in Fig. 16, is defined by:

$$E_{\rm rel} = m_{B^*}c^2 - m_c c^2 - m_d c^2. \tag{23}$$

The excitation energy of the nucleus B can then be deduced from:

$$E_x = m_{B^*}c^2 - m_B c^2 = E_{\rm rel} + E_{\rm th}. \tag{24}$$

with $E_{\rm th} = (m_c c^2 + m_d c^2) - m_B c^2$ being the separation energy of the cluster system.

Similar to the description in the MM method, the Q-value of the reaction–decay process, as illustrated in Fig. 16 and corresponding to the mass deficit of the initial two-body channel and the final three-body channel, can also be deduced from the measured energy–momentum of the particles involved. If such a measured Q-value is smaller than the g.s. Q-value, then excitation can be expected in some of the final nuclei.

3.2.2 Useful observations

In the analysis of reaction–decay processes, as depicted in Fig. 16, some quantities (observables) are useful and often employed to clarify the true process or structural effects, such as the energy–momentum (E–P) plot, monopole transition strength, angular correlation analysis, cluster spectroscopic factor. A brief outline of these quantities is given below.

E–P plot for target component selection

In a real experiment, some composite materials may have to be used for targets, such as $(CH_2)_n$ and $(CD_2)_n$. In such cases, the accurate differentiation of the recoil target nucleus is crucial to obtain the clear Q-value spectrum and the excitation-energy spectra [143, 144]. The E–P plot is an effective method for selecting the target component based on the measured quantities [50, 145]. Defining x and y from the measured quantities:

$$\begin{aligned} x &= \boldsymbol{p}_b^2/2u \\ y &= T_b - Q = T_A - T_c - T_d \end{aligned} \tag{25}$$

where u is the known atomic mass unit, and $\boldsymbol{p}_b^2$ can be deduced from the momentum of the beam and the two decay particles, according to the momentum conservation. For the

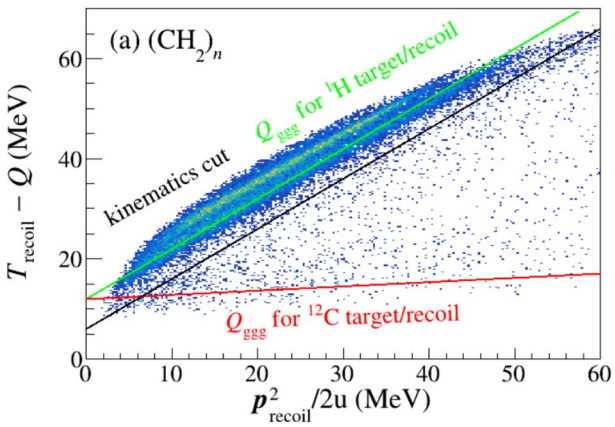

Fig. 17 (Color online) E–P plot of the reaction $^{14}C + (CH_2)_n$. See Sect. 3.2 on the EP-plot for details. This figure was taken from Ref. [146]

recoil nucleus with mass number A_b, the kinetic energy can be expressed as $T_b = \frac{1}{A_b}\frac{p_b^2}{2u}$. The two-dimensional plot of y versus x, known as the E–P plot, follows the linear relation $y = x/A_b - Q$, with the slope parameter $1/A_b$ characterizing the actual target nucleus and the intercept of the respective Q-value. Figure 17 shows the E–P plot for a $^{14}C + (CH_2)_n$ experiment [146] in which three bands with a slope of approximately 1 correspond to an H target but the decay fragment ^{10}Be in its ground, 2_1^+, and ~ 6 MeV excited states, respectively. The red line in Fig. 17, with a slope of ~ 1/12, indicates the contribution from the carbon target. Thus, the cut on E–P plot provides a target component selection. The quality of the E–P plot depends on the energy resolutions of the detected particles and the beam particles. When using RIBs with a large beam-energy spread, it would be difficult to make a specific cut on the E–P plot. Also, in the case of the target–nucleus breakup during the reaction, which often occurs in cases involving deuteron or carbon targets, the resolution of the E–P plot deteriorates.

Monopole transition strength

As described in Sect. 2.4 for GTCM, the enhanced monopole-transition strength between two nearby 0^+ states is an imprint of the cluster formation [90]. Experimentally, the extraction of the monopole-transition matrix element from either the electromagnetic process [M(E0)] or nuclear process [M(IS, 0)] is an important aspect of a cluster structure study. These matrix elements are defined in the following forms [147, 148]:

$$\begin{aligned} M(\mathrm{E0}) &= \left\langle f \left| \sum_{i=1}^{A} \frac{1+\tau_{3i}}{2} (\boldsymbol{r}_i - \boldsymbol{R}_{\mathrm{c.m.}})^2 \right| \mathrm{g.s.} \right\rangle, \\ M(\mathrm{IS}, 0) &= \left\langle f \left| \sum_{i=1}^{A} (\boldsymbol{r}_i - \boldsymbol{R}_{\mathrm{c.m.}})^2 \right| \mathrm{g.s.} \right\rangle, \end{aligned} \tag{26}$$

where τ_3 is the isospin projection operator and f denotes the excited 0^+ states. The energy-weighted sum rule (EWSR) for the isoscaler transition S(IS, 0) is given by [149]:

$$S(\mathrm{IS}, 0) = \sum_f |M(\mathrm{IS}, 0)|^2 E_f = \frac{2\hbar^2}{m} A R_{\mathrm{rms}}^2. \tag{27}$$

The isoscalar monopole transition is generally treated in the framework of the breathing mode oscillation, which can be analyzed within the optical model [148, 150]. The transition potential $G_0(r)$ is expressed as [150]:

$$G_0(r) = -\alpha_0^U \left[3U(r) + r\frac{\mathrm{d}U(r)}{\mathrm{d}r} \right], \tag{28}$$

where $U(r)$ is the standard optical potential and α_0^U is the amplitude parameter. The transition matrix element can be acquired via a multipole decomposition (MD) analysis of inelastic differential cross-sections [151, 152]:

$$\left(\frac{\mathrm{d}\sigma}{\mathrm{d}\Omega}\right)_{\mathrm{exp}} = \sum_L a_L \left(\frac{\mathrm{d}\sigma}{\mathrm{d}\Omega}\right)_{L,\mathrm{DWBA}}, \tag{29}$$

where $(\frac{\mathrm{d}\sigma}{\mathrm{d}\Omega})_{\mathrm{exp}}$ are the experimental data and $(\frac{\mathrm{d}\sigma}{\mathrm{d}\Omega})_{L,\mathrm{DWBA}}$ represents the cross-section calculated under the distorted-wave Born approximation (DWBA) for a transferred angular momentum L. Here, a_L can be obtained via a fitting procedure corresponding to the fraction of EWSR for a monopole ($L = 0$) or multipole ($L > 1$) transition [153].

In 2014, an experimental method by which to extract the monopole transition strength using inelastic scattering data was established [46]. Figure 18 shows the experimental differential cross-sections for the 10.3 MeV (0_3^+) state of ^{12}Be. The cross-sections were reproduced by the DWBA calculations with a normalization factor of $a_0 = 0.034(10)$, which is associated with the EWSR fraction (6727.9 fm^4 MeV^2). The deduced monopole transition matrix element (M(IS)) is 7.0 ± 1.0 fm^2, which is comparable to those of typical cluster states [90, 154, 155].

Angular correlation analysis

Spin is always an important quantity in nuclear structure characterization. In the case of a cluster or molecular structure, spin-parity determination is a precondition to addressing the excitation and decay modes as well as allocating the members in a rotational band. In early inclusive MM experiments, the spin of a produced recoil nucleus associated with transferred orbital angular momentum [137] is typically determined by measuring the angular distribution of the probe. However, this approach is valid only for direct reactions (scattering) to low lying states, and it is questionable when applied to highly

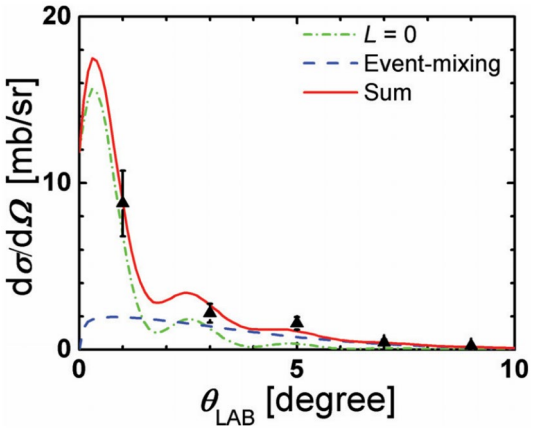

Fig. 18 (Color online) Experimental differential cross-sections compared with the DWBA calculations for the 10.3 MeV state in ^{12}Be, as reconstructed by the ^{4}He + ^{8}He decay channel. This figure was taken from Ref. [153]

excited resonant states. Fortunately, the resonance-decay provides another independent and effective means by which to determine the spin of the mother nucleus, regardless of its production mechanisms [44, 46, 49, 102, 103, 142, 153, 156–158].

By assuming a two-step process for the resonance production and decay, as depicted in Fig. 16 for the resonant nucleus B^*, the conservation of the total angular momentum adheres to:

$$\begin{aligned} \boldsymbol{l}_i + \boldsymbol{J}_A + \boldsymbol{J}_a &= \boldsymbol{J}_{B^*} + \boldsymbol{J}_b + \boldsymbol{l}_f \\ \boldsymbol{J}_{B^*} &= \boldsymbol{J}_c + \boldsymbol{J}_d + \boldsymbol{l}', \end{aligned} \tag{30}$$

where $\boldsymbol{l}_i$ and $\boldsymbol{l}_f(\boldsymbol{l}')$ represent the orbital angular momentum of the incident and decay channels, respectively, and $\boldsymbol{J}_i$ ($i = A, a, B^*, b, c, d$) denotes the spin of the corresponding nucleus. In the Cartesian coordinate system, the conservation of the angular momentum in the z (beam) direction can be expressed as $m_i + m_A + m_a = m_{B^*} + m_b + m_f$ and $m_{B^*} = m_c + m_d + m'$, where $m_i = 0$ as the z direction is the same as that in the beam direction. The double-differential cross-section can be expressed as the product of the transition amplitudes for the formation ($T^{m_a m_A}_{m_b m_{B^*}}(\Omega^*)$) and decay ($T^{m_{B^*}}_{m_c m_d}(\Omega_\psi)$) [159, 160]:

$$\frac{\mathrm{d}^2\sigma}{\mathrm{d}\Omega^*\mathrm{d}\Omega_\psi} \propto \sum_{m_a m_A m_c m_d m_b} \left| \sum_{m_{B^*}} T^{m_a m_A}_{m_b m_{B^*}}(\Omega^*) T^{m_{B^*}}_{m_c m_d}(\Omega_\psi) \right|^2. \tag{31}$$

If the spins of the decaying daughter nuclei (c and d), projectile nucleus (A), target nucleus (a), and recoil nucleus (b) are all zero, then the spin of the compound nucleus B^* is determined by the change of the orbital angular momentum before and after the reaction. In this case, Eq. 31 can be simplified as:

$$\frac{\mathrm{d}^2\sigma}{\mathrm{d}\Omega^*\mathrm{d}\Omega_\psi} \propto \left| \sum_{m_{B^*}} T^{J_{B^*}}_{m_{B^*}}(\Omega^*) Y^{m_{B^*}}_{J_{B^*}}(\Omega_\psi) \right|^2. \tag{32}$$

In the strong absorption approximation, the incident channel is dominated by a peripheral partial wave l_i. Then [159]:

$$\begin{aligned} T^{J_{B^*}}_{m_{B^*}}(\Omega^*) &= \sum_{m_f} C Y^0_{l_i}(0,0) Y^{m_f}_{l_f}(\theta^*, \phi^*) \\ &= C' Y^0_{l_i}(0,0) Y^{m_f=-m_{B^*}}_{l_f}(\theta^*, \phi^*), \end{aligned} \tag{33}$$

where C and C' are given by $\langle J_{B^*}, m_{B^*}, l_f, m_f | l_i, 0\rangle$ and $\langle J_{B^*}, m_{B^*}, l_f, m_f = -m_{B^*} | l_i, 0\rangle$, respectively. The peripheral partial wave angular momentum of the incident channel is $l_i = r_0(A_p^{1/3} + A_t^{1/3})\sqrt{2\mu E_{\mathrm{c.m.}}}$.

According to the relation between the primary reaction and sequential decay processes, angular correlations can be divided into in-plane and out-of-plane correlations. The correlation angles are defined in Fig. 1 of Ref. [159]. In-plane correlation refers to the alignment between the decay plane and the reaction plane, where the azimuthal angle χ is constrained around 0° or 180°. The double-differential cross-section only depends on the scattering angle θ^* and decay angle ψ. In some experiments [142, 157–166], owing to the geometric arrangement of the detectors, both the reaction and decay planes closely align with the detector plane, thereby satisfying the conditions for in-plane correlation. When the spins of the initial and final-state particles are zero, the events of in-plane correlation exhibit a linear "ridge" structure in the $\theta^* - \psi$ plot, which is commonly employed in spin analyses [158–160, 162–164]. This linear "ridge" structure is described by the following function:

$$W(\theta^*, \psi) \approx W(\theta^{*\prime} = 0, \psi' = \psi - \theta^*/a). \tag{34}$$

Here, $a = J_{B^*}/(l_i - J_{B^*})$ is related to the spin J_{B^*} of the compound nucleus B^* and orbital angular momentum l_i of the incident channel. When the $\theta^* - \psi$ correlation structure of the differential cross-section in the $\theta^* - \psi$ plane is projected onto $\theta^{*\prime} = 0°$, it follows the $|P_{J_{B^*}}(\cos\psi')|^2$ distribution.

The reason for the appearance of the linear "ridge" structure in the in-plane correlation is that when the spins of all the initial and final particles are zero, the spin $\boldsymbol{J}_{B^*}$ of B^* can be determined by the change of orbital angular momentum ($\boldsymbol{J}_{B^*} = \boldsymbol{l}_i - \boldsymbol{l}_f$). Moreover, there is a strong coupling between $\boldsymbol{J}_{B^*}$ and the final-state orbital angular momentum $\boldsymbol{l}_f$ in their orientations ($m_{B^*} = -m_f$). Rae and Marsh also provided rigorous derivations of this phenomenon from a quantum mechanical perspective [160, 167]. Hence, substituting Eq. 33 for the transition amplitude of compound nucleus formation into Eq. 32 for the differential cross-section:

$$\frac{\mathrm{d}^2\sigma}{\mathrm{d}\Omega^*\mathrm{d}\Omega_\psi} \propto \left| \sum_{m_{B^*}} C' Y^0_{l_i}(0,0) Y^{m_f=-m_{B^*}}_{l_f}(\theta^*, 0) Y^{m_{B^*}}_{J_{B^*}}(\psi, 0) \right|^2. \tag{35}$$

When the spins of the projectile, target, and recoil nucleus are nonzero, the spin $\boldsymbol{J}_{B^*}$ of the compound nucleus B^* may be influenced not only by the change of orbital angular momentum but also by the change of spins between nuclei that are involved before and after the reaction. According to Eq. 30, the expressions for the transition amplitude (Eq. 33) and differential cross-section (Eq. 35) include the coupled terms $Y^{m_f \neq -m_{B^*}}_{l_f}(\theta^*, 0) Y_{J_{B^* m_{B^*}}}(\psi, 0)$ with $m_{B^*} \neq -m_f$. These coupled terms introduce additional data points that fill in between the peaks of the linear "ridge" structure, thereby reducing or even completely erasing the prominence of the "ridge" pattern. Some experiments with a significant number

of nonzero spins for the projectile, target, or recoil nucleus have revealed clear in-plane angular correlation structures [142, 157, 164]. Hence, the proportion of data points contributed by these coupled terms is critical.

In the case of out-of-plane correlation, the angular difference between the decay plane and the reaction plane is significant, indicating a large deviation of the χ angle from 0° or 180°. For instance, a wider range of ϕ^* and χ angles could be covered by employing detectors with larger sensitive areas or placing them closer to the target [159]. Another example comes from the use of a zero-degree detector that covers $\theta^* \sim 0°$ as well as the entire ranges of ϕ^* and χ angles [46, 49, 153, 168]. In the case of spin-0 for all initial and final particles, the "ridge" structure on the $\theta^* - \psi$ plot deviates from linearity [159], making it unsuitable for spin analysis. To enhance the structure in cases of out-of-plane correlation, additional constraints (projections) are typically needed. There exist two experimental cases that may greatly simplify the analysis of the angular correlation [159]. The first involves the zero-degree measurements ($\theta^* \sim 0°$), where the motion of the compound nucleus B^* and relative motion between B^* and b are almost aligned along the z-axis, resulting in $m_f = 0$ and $m_{B^*} = m_0 = 0$ (where ψ is not necessarily equal to 0). Therefore, the differential cross-section distribution follows the square of a Legendre polynomial and is solely correlated with ψ in the form:

$$\frac{\mathrm{d}^2\sigma}{\mathrm{d}\Omega^*\mathrm{d}\Omega_\psi} \propto |P_{J_{B^*}}(\cos\psi)|^2. \tag{36}$$

In resonant scattering experiments with no recoil particle b, the condition of zero-degree measurement ($\theta^* \sim 0$) is automatically satisfied. This result is helpful in the determination of the spin [102, 103], although the background counting is often high due to the mixing of the non-resonant processes. Another case involves verifying whether the spin of the compound nucleus, denoted by $\boldsymbol{J}_{B^*}$, is 0. If so, then the decay process is independent of the decay angle and the distribution on Ψ is naturally uniform. Otherwise, if $\boldsymbol{J}_{B^*}$ is nonzero, it becomes necessary to select data within the reaction plane and apply rigorous angular corrections to accurately determine the spin of the resonant state [46, 49, 153, 168]. The determination of the spins of members of the linear chain rotational band in ^{14}C provides an excellent example of this scenario [50].

Cluster spectroscopic factor

In a nuclear state, the cluster structure might be mixed with other configurations, such as shell-like contents. Therefore, it is important to quantify the probability of having the cluster structure in an energy eigenstate. This has been realized in the literature by using the cluster spectroscopic factor within the R–matrix framework [169]. First the cluster-decay partial width, which is the product of the spectrum-extracted (BW form) total width of the resonance and the fraction of the IM-reconstructed cluster cross-section over the total MM cross section, should be determined experimentally. Within the single-channel R–matrix approach, this measured partial cluster width, denoted by $\Gamma_\alpha(E)$, can be related to the reduced width γ_α^2 and barrier penetrability factor $P_l(E)$, according to [170, 171]:

$$\Gamma_\alpha(E) = 2\gamma_\alpha^2 P_l(E), \tag{37}$$

with

$$P_l(E) = \frac{ka}{(F_l(ka))^2 + (G_l(ka))^2}. \tag{38}$$

Here E is the decay energy (or relative energy), and a is the channel radius. The latter is generally given by $a = r_0(A_1^{1/3} + A_2^{1/3})$ with $r_0 \approx 1.4$ fm (although this may vary for exotic structures). In addition, $F_l(ka)$ and $G_l(ka)$ represent regular and irregular Coulomb wave functions, respectively [170, 171]. The γ_α^2 term is usually compared with the Wigner limit γ_W^2 to give the dimensionless reduced width θ^2, which is close to 1 for a strong cluster structure:

$$\theta_\alpha^2 = \frac{\gamma_\alpha^2}{\gamma_W^2}, \quad \text{with } \gamma_W^2 = \frac{3\hbar^2}{2\mu a^2}. \tag{39}$$

where θ_α^2 is also known as "the cluster spectroscopic factor" and represents the probability for finding the corresponding clusters in the resonant state. As references, $\theta_\alpha^2(^8\mathrm{Be}, \mathrm{g.s.}) \approx 0.45$ [19] and $\theta_\alpha^2(^{12}\mathrm{Be}, 0_3^+(10.3\ \mathrm{MeV})) \approx 0.53$ [168].

3.2.3 Experimental investigations of cluster structures

Over the past three decades, there have been a growing number of experiments studying nuclear cluster structures by utilizing the IM method. The detection systems were mostly composed of position-sensitive silicon detectors with advanced data acquisition systems [172–174] to measure multiple particles in coincidence and with high resolution. These experiments encompass a wide range of reaction types, including the inelastic scattering, transfer reaction, and resonant scattering. The important criteria for identifying the cluster (molecular) structure in a nucleus include the extremely large moment of inertia deduced according to the energy-spin systematics for a rotational band, relatively large cluster decay width or cluster spectroscopic factor, enhanced characteristic (e.g., isoscalar monopole) transition strength, and selective decay paths. All these criteria depend on the cluster decay measurement and spin determination. Because a single experiment may not be able to

obtain all these quantities, complementary works are generally required. We outline a few selected experimental works here to demonstrate the major progress made regarding IM measurements.

Studies on cluster structure in beryllium isotopes

The neutron-rich Be isotopes possess an inherent two-center feature, considering the unambiguous 2α structure of ^{8}Be. The clustering configurations and the molecular rotational bands in ^{10}Be have been intensively been studied since the 1990s [3, 44, 45]. Here, we focus on ^{12}Be to demonstrate the recent experimental progress.

In 1999, Freer et al. conducted an inelastic breakup experiment for ^{12}Be at 31.5 MeV/u on a $(CH_2)_n$ target [175]. They utilized silicon telescopes to measure helium fragments and reconstruct ^{12}Be resonant states via the ^{4}He + ^{8}He and ^{6}He + ^{6}He decay channels. They successfully observed a few cluster states above 13.2 MeV and with spins J exceeding 2. Figure 19 (c) and (d) display the IM spectra for these decay channels. Subsequently, several experiments employed the IM method to further investigate the highly excited cluster states in ^{12}Be. However, despite all efforts, the identification of the band head state, which should be closer to the cluster separation threshold, remained elusive throughout the following decade [176].

Significant progress was made by Yang et al. in 2014 through a novel inelastic scattering experiment of ^{12}Be at 29 MeV/u on a carbon target [46, 153]. A major difference compared with the previous experiment was the use of a zero-degree telescope composed of high-performance silicon-strip detectors that substantially improved detection efficiency at energies close to the threshold, as displayed in Fig. 19(b) (dotted line). This experiment enabled

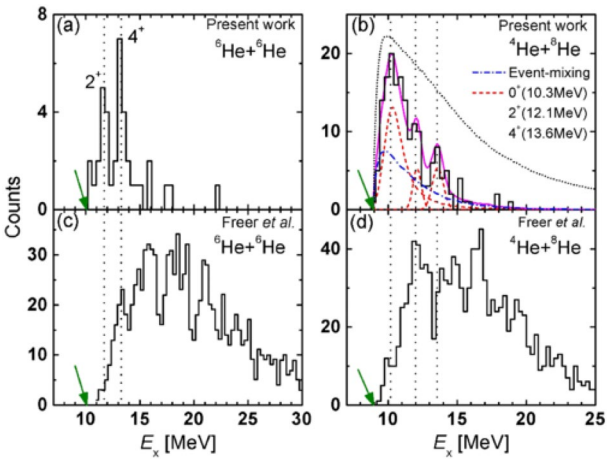

Fig. 19 (Color online) Excitation energy spectra of ^{12}Be reconstructed from the **a**, **c** ^{6}He + ^{6}He and **b**, **d** ^{4}He + ^{8}He decay channels. The spectra in the upper panels (**a**, **b**) are from Ref. [46], and those in the lower panels (**c**, **d**) are from Ref. [143]

identification of the band head (10.3 MeV) of the ^{4}He + ^{8}He molecular rotational band. Furthermore, the spin-parity of this state was firmly assigned as 0^{+}, based on the angular correlation analysis, associated isoscalar monopole transition strength, and extracted cluster spectroscopic factor. All these criteria consistently support the dominant ^{4}He + ^{8}He cluster structure in this prominent and near-threshold resonance [46, 153, 168].

Studies on cluster structures in carbon isotopes

Owing to the possibility of 3α cores, more abundant cluster structures can be expected for carbon isotopes, including the triangle and linear chain configurations [3, 41, 65, 66, 99, 177–179]. Compared with prior work on beryllium isotopes with 2α cores, experimental investigations of carbon systems are more challenging. Here, the decay fragments, such as ^{10,12}Be, may possess bound excited states. Hence, the conversion from the measured relative energy spectrum to the physically meaningful excitation energy spectrum necessarily depends on the specific states of the decaying fragments, corresponding to different Q-values (or total energies in the final channel) [48–50]. A series of breakup reaction experiments (Fig. 16) that were dedicated to the simultaneous reconstruction of the relative energy and reaction Q-value have been performed to search for the exotic cluster structures in carbon isotopes [48, 158, 180–185]. These measurements generated consistent resonant energies but little information on the spin-parities, primarily due to the limited resolutions or statistics [183, 186]. Traditional resonant scattering experiments using the thick-target (^{4}He gas) technique played an important role in the study of Be isotopes but were not able to measure the reaction Q-values and hence may have overlapped the excitation-energy spectra for different threshold energies [47, 102, 103]. Therefore, the high resolution Q-value spectrum is crucial when studying the cluster structure in carbon or heavier isotopes, especially when determining the correct application of the decay path analysis [49, 156].

The linear chain structure was initially proposed for the 0^{+}_{2} state of ^{12}C (the Hoyle state) [51]. Previous studies have revealed the instability of the chain structure in ^{12}C [99, 177]. Hence, it is crucial to search for linear chain molecular bands in ^{14,16}C. One major step forward was made by Liu et al. in their work on the inelastic scattering of ^{16}C at 23.5 MeV/nucleon on $(CD_2)_n$ targets [49, 156]. As illustrated in Fig. 16, in previous IM experiments, it is typical to measure only two of the three final particles (particles b, c, and d) [157, 184]. The energy of the remaining particle is deduced according to the conservation of momentum by considering the beam energy. Because the PF-type RIB used to have a large energy spread, the obtained Q-value spectrum did not have a sufficient energy resolution [184]. In novel new inelastic scattering experiment for ^{16}C conducted

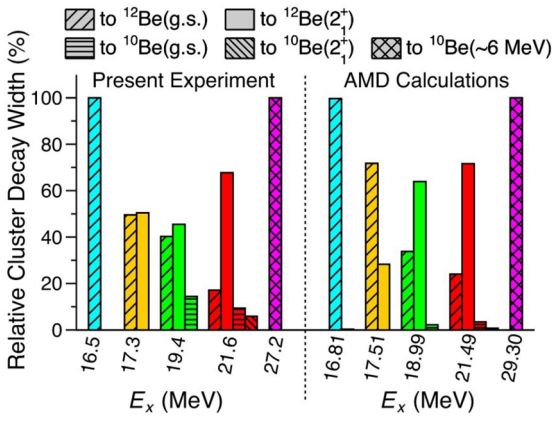

Fig. 20 (Color online) Relative cluster decay widths from the resonant states in ^{16}C to the ^{12}Be (+ ^{4}He) and ^{10}Be (+ ^{6}He) final channels, as obtained from the experiment reported in Ref. [49] (left panel), compared with calculations performed via the AMD approach [66] (right panel). This figure was taken from Ref. [49]

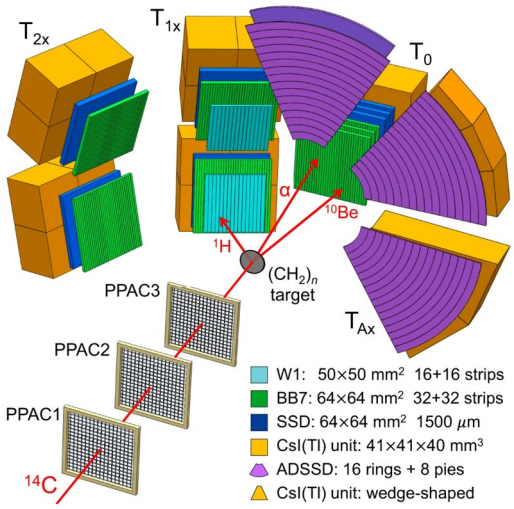

Fig. 21 (Color online) Schematic view of the detection system for the ^{14}C experiment. The ^{14}C beam particles (red line) are tracked by three parallel plate avalanche chambers (PPACs), and the interested final particles (red arrows) are detected by different telescopes consisting of double-sided silicon strip detectors (DSSDs and ADSSDs), large-size silicon detectors (SSDs), and CsI(Tl) scintillators. This figure was taken from Ref. [50]

by Liu et al. [49, 156], all three final particles were coincidentally detected using high-resolution silicon detectors. Hence, the beam energy could be deduced event-by-event from the final particles, based on the momentum conservation. This way, the obtained Q-value spectrum resolution does not depend on the RIB quality and instead depends only on the detector performance. In addition, a state-of-the-art analysis method was developed to recover events with two nearby fragments hitting adjacent strips of the detector. The zero-degree telescope composed of multilayer silicon-strip detectors played an essential role in this experimental use of RIB in inverse kinematics. The high resolution Q-value spectra have enabled the clear selection of the decay paths from the ^{16}C resonances to various states of the final fragment ^{10}Be (+ ^{6}He) or ^{12}Be (+ ^{4}He). Figure 20 shows the observed relative decay strengths for different decay paths. The excellent agreement between the observed and predicted characteristic decay patterns gives, for the first time, strong evidence for the existence of the linear chain configuration in ^{16}C. In addition, the experimental determination of the spin-0 for the 16.5 MeV band head provides further support for the chain-type molecular rotational band. These assigned band members correspond to the $(3/2^-_\pi)^2(1/2^-_\sigma)^2$ valence neutron configuration. A tentative state at approximately 27.2 MeV also hints at the possible existence of the pure σ-bond configuration, although this phenomenon requires further investigation.

Subsequently, a similar inelastic scattering experiment was also conducted for ^{14}C at 23.0 MeV/nucleon on $(CH_2)_n$ targets [50]. Proton targets were chosen here, at the expense of lower c.m. energy, to provide a better energy resolution and avoid the target breakup effect as significantly occur for deuteron target. The complex experimental setup, centered around the zero-degree telescope composed of multilayer-silicon-strip detectors, is schematically shown in Fig. 21. Again, three-fold coincidence measurements were realized for all final particles (^{4}He and ^{10}Be decay fragments plus the recoil proton), providing an almost background-free and high-resolution Q-value spectrum as well as well-established resonant states in ^{14}C. One state at 13.9 MeV was firmly identified for the first time. The contribution of this work is its determination the spin-parities of the 13.9 MeV, 14.9 MeV, and 17.3 MeV states based on the clear angular correlation analyses and differential cross-section analyses (Fig. 22). These states agree excellently with the members of the predicted linear chain molecular rotational band with the π^2-bond configuration.

There are also several experimental works devoted to the study of cluster structures for other carbon isotopes, such as ^{11}C [187], ^{13}C [79], and its mirror nucleus ^{13}N [188]. Abundant cluster (molecular) configurations have also been unveiled in these nuclei.

Studies on BEC-like structures

As indicated in Sect. 2.6, the concept of BEC-like states in nuclei was initially raised and accepted in the literature for the 0^+_2 state of ^{12}C, which is commonly known as the "Hoyle state" [18]. A comprehensive summary of measurements related to the properties of the Hoyle state are provided in Ref. [19]. However, many of these measurements

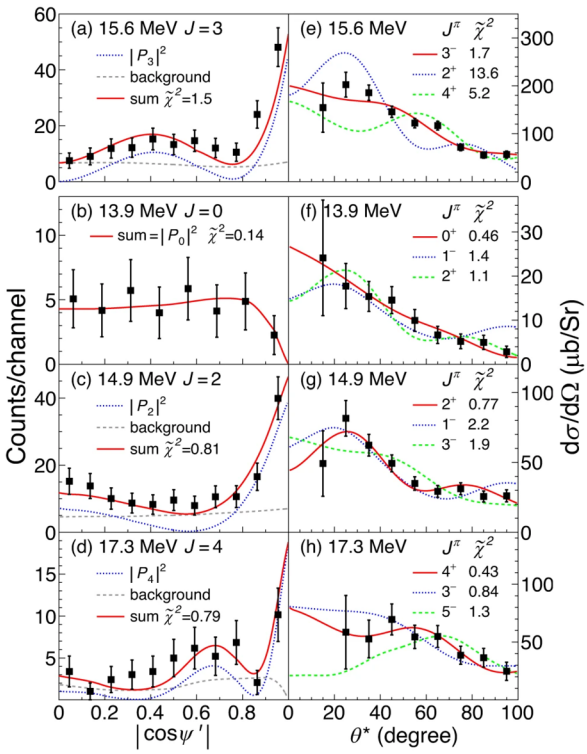

Fig. 22 (Color online) Angular correlation and differential cross-section spectra for the 15.6 MeV, 13.9 MeV, 14.9 MeV, and 17.3 MeV resonances in ^{14}C. The data are shown as black squares. **a**–**d** Each measured angular correlation spectrum is compared to a Legendre polynomial of order $J = 3$, 0, 2, or 4 (represented by the blue-dotted lines), respectively, plus a constant background (represented by the gray-dashed line). **e**–**h** Data for the differential cross-sections fitted using the DWBA calculations under different spin-parity assumptions. This figure was taken from Ref. [50]

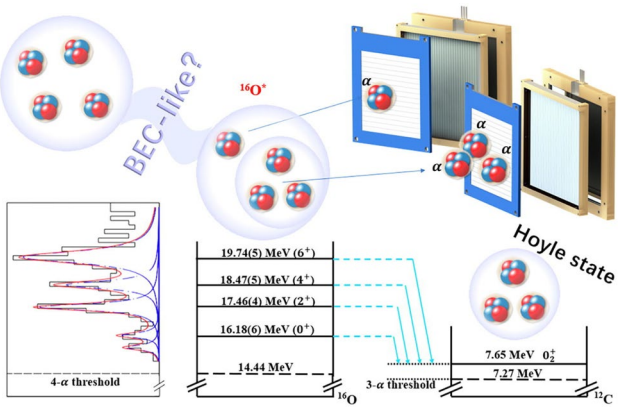

Fig. 23 (Color online) Schematic illustrating the observed $^{12}C(0_2^+) + \alpha$ resonant states in ^{16}O. The detection system consisted of eight sets of charged particle telescopes, symmetrically installed on both sides of the beam axis (illustrated here with only two sets). Four narrow resonances immediately above the 15.1 MeV state were firmly identified after selecting the $^{12}C(0_2^+) + \alpha$ decay channel. This figure was taken from Ref. [28]

are indirect and require theoretical models to make connections with the internal structure. For instance, the inelastic scattering form factor is sensitive to the size of the final excited state, and these results provide strong evidence for the presence of an expanded gas-like structure within the Hoyle state [3, 16, 92, 189–191].

It is natural to anticipate more BEC-analog structures in other nuclei, such as ^{16}O, ^{20}Ne, and ^{24}Mg. However, experimental studies on these heavier systems face more challenges due to the requirement of simultaneous detection and identification of more bosonic particles in the final state. Recently, the 0_6^+ state at 15.1 MeV in ^{16}O, located immediately above the 4α separation threshold at 14.4 MeV, has attracted significant attention, owing to its predicted BEC-analog structure [38, 192, 193]. Previous experiments [194–196] relied on only partial α-PID, resulting in high background levels in the E_x spectra. This background contamination has hindered the possible 4α resonant states [194–197].

In a recent inelastic excitation decay experiment for ^{16}O [28], four α-particles in the final channel were fully detected and clearly identified. By selecting events with 3α forming the Hoyle state of ^{12}C and the remaining one as a valence particle, the reconstructed IM spectrum of ^{16}O exhibits four narrow resonances located immediately above the $\alpha + {}^{12}C(0_2^+)$ decay threshold, as shown in Fig. 23. These observed 4α resonant states are in good agreement with the results of theoretical calculations [198], which suggest the existence of a rotational band having the $^{12}C(0_2^+) + \alpha$ molecular configuration and band members of 0^+, 2^+, 4^+, and 6^+ at energies similar to those of the present observations. Within this molecular band, the 0^+ band head can naturally be considered as a BEC-analog state. Further measurements to directly determine the spins of these resonances in ^{16}O will be of great value.

Some pioneering experiments have also been performed to probe multi-α, BEC-like states in heavier systems [199], including ^{20}Ne [111, 200], ^{24}Mg [201–203], ^{28}Si [204, 205]. The measurement of α-cluster formation and decay from heavy nuclei have also been advanced in recent years [206–209].

A new form of BEC in the nuclear system is related to the ^2n cluster in low-density environments. After the discovery of the two-neutron (2n) halo in the mid-1980s, the concept of neutron halo was proposed, based on the idea of valence-neutron clustering in neutron-rich nuclei, such as ^{11}Li [52, 210]. It has been gradually realized that ^2n-formation can be enhanced at the surface of neutron-rich nuclei or in the inner crust layers of neutron stars [53–58]. Moreover, ^2n is defined as a spatially compact entity with a size of $2 \sim 5$ fm, comprising a spin-singlet neutron pair in an internal s-orbital that behaves like a boson. Therefore, in very neutron-rich nuclei, numerous

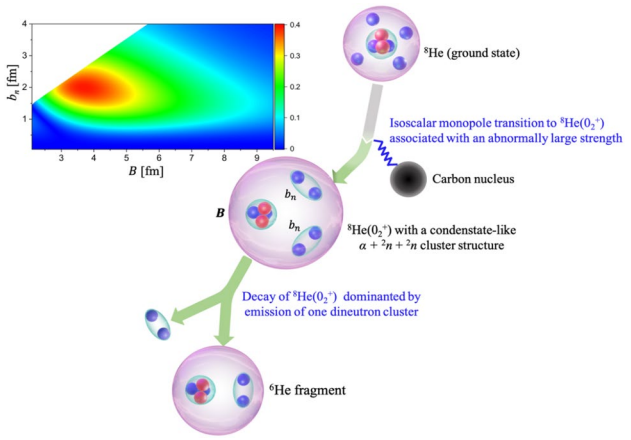

Fig. 24 (Color online) Schematic of the population and decay of the ^{8}He(0^+_2) state. The ^{8}He(0^+_2) state [59, 94] is populated via an isoscalar monopole transition induced by a carbon target nucleus and then decays predominantly via the emission of a neutron pair. The inset shows the overlap of the w.f. of the predicted ^{8}He(0^+_2) state, as calculated using the microscopic $\alpha + 4$n model, with the condensate-like $\alpha + {}^2n + {}^2n$ (THSR) w.f. specified by the nucleus size parameter B and dineutron (^2n) size parameter b_n. This figure was taken from Ref. [60]

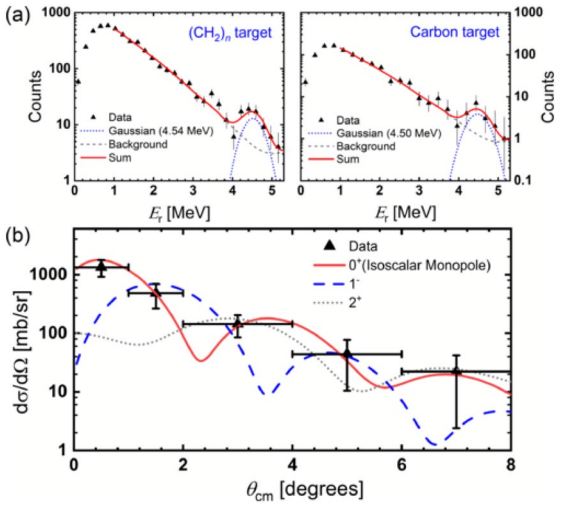

Fig. 25 (Color online) **a** Relative energy E_r spectra for $(CH_2)_n$ and carbon targets (c.m. scattering angle $\theta_{c.m.} < 2°$), fitted using a Gaussian peak and second-order polynomial background, modified by the acceptance. **b** Angular distribution of the 4.5-MeV state for the $(CH_2)_n$ target. This figure was taken from Ref. [60]

excessive neutrons at the surface of the nucleus might form a ^2n-BEC-analog state. Experimentally, it is interesting to investigate the ^{8}He system, which might be the lightest one composed of multi-^2n in the BEC configuration [59]. Recently, an inelastic scattering experiment was performed using an intense ^{8}He beam at 82.3 MeV/nucleon [211]. The decay products ^{6}He + 2n were detected with high precision (Fig. 24). One important contribution of this work is the clarification of the excitation-decay mechanism via the application of a novel angular correlation analysis method that enabled the significant reduction of background events resulting from direct breakup processes [60]. The emergence of a prominent peak at a relative energy of 4.54 (6) MeV was then observed with a high significance level, as displayed in Fig. 25 (a). Combining these results with the spin determination, monopole-transition analysis, and $2n$-correlation analysis, this resonant state can be classified as the 0^+_2 state of ^{8}He [Fig. 25 (b)], which possesses the predicted BEC-like configuration [59, 60]. This groundbreaking observation is encouraging for the future exploration of ^2n-BEC states in heavier neutron-rich nuclei and neutron stars.

3.3 Resonant scattering and thick target method

The resonant scattering method can be regarded as a variant of the IM method. It typically utilizes a thick gas target in which the beam particle loses energy as a function of the track depth. When the center-of-mass energy of the beam–target system coincides with the corresponding resonant energy of the compound nucleus, the reaction cross-section may suddenly increase. Then, the unstable compound nucleus decays back to the projectile and target nuclei. To satisfy the conditions of the inverse kinematics, the beam particle should be heavier than the target. This allows the light fragments to penetrate a sufficient depth into the gas to reach the particle detectors [19, 202]. The excitation energy of the compound nucleus can then be deduced by measuring the energy of the fragments. In these experiments, silicon detectors are commonly placed in a gas-filled target chamber. Figure 26 illustrates a typical setup for a resonant scattering experiment.

Using resonant scattering setups, several experiments have been conducted to investigate nuclear cluster structures, including the ^{6}He +^{4} He configuration in ^{10}Be [44], ^{15}O + α in ^{19}Ne [212], and ^{14}C + α in ^{18}O [213]. Usually, the R–matrix calculation is required to fit the spectrum and

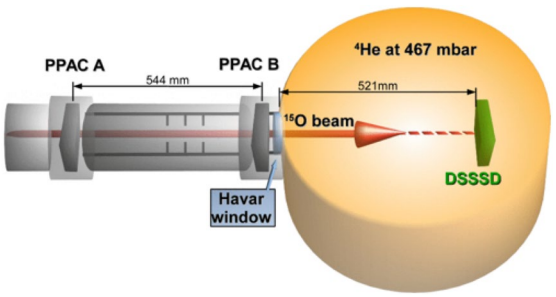

Fig. 26 (Color online) Illustration of the experimental setup for a typical resonant scattering experiment. The detection system consisted of one DSSD and two PPACs. This figure was taken from Ref. [212]

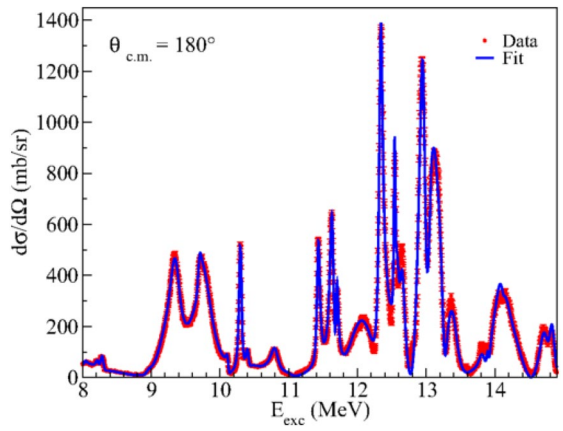

Fig. 27 (Color online) Excitation function measured from the $^{14}C + \alpha$ resonant scattering [213]. The solid curve shows the best fit using the *R*–matrix calculation

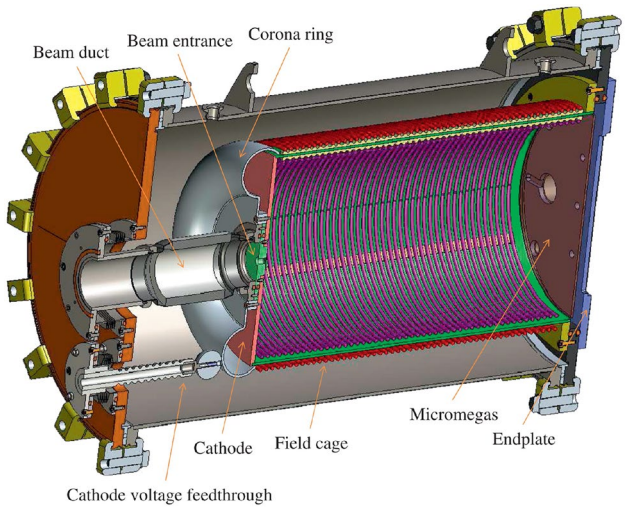

Fig. 28 (Color online) Schematic of the cross-section of a prototype AT-TPC. The AT-TPC is equipped with a cylindrical field cage filled with the active gas, which serves as both a tracking medium and a reaction target. This figure was taken from Ref. [214]

extract the resonance parameters (configurations, energies, spin-parities, widths, etc.), as demonstrated in Fig. 27.

The limited resolution of the reaction position within the thick target and interference from inelastic scattering can introduce large uncertainties in the determination of the resonant states. The situation may become more serious when the final fragments have bound excited states, as the determination of the reaction position might be mixed with the determination of the excited states of the final particle [49, 50]. This problem can be resolved by employing the active target time projection chamber (AT-TPC) which may independently recognize the reaction position without relying on particle energy detection [214–216]. These results are due to the tracking capability of the TPC

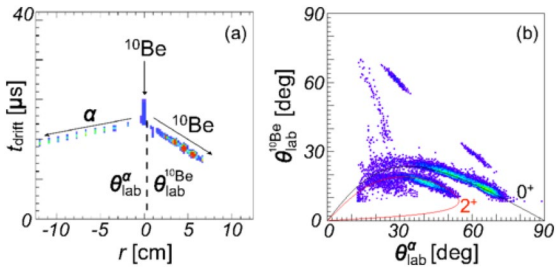

Fig. 29 (Color online) **a** Trajectories of ^{10}Be + ^{4}He resonant scattering. **b** Kinematical correlation of the angle θ_{lab} between ^{10}Be and ^{4}He. This figure was taken from Ref. [103]

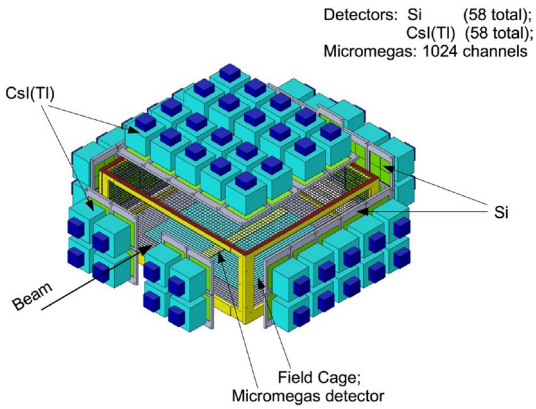

Fig. 30 (Color online) Schematic of combined TPC-telescopes. The TPC is encircled by an array of 58 Si-CsI(Tl) telescope detectors and covers a total solid angle of approximately 3π. This figure was taken from Ref. [217]

in addition to the energy measurements. Figure 28 shows a schematic for a typical AT-TPC setup.

The resonant scattering experiment conducted by Fritsch et al. in 2016 on the ^{10}Be + ^{4}He system [103] is a notable example. The trajectories of the initial and final state particles were recorded in an AT-TPC, as depicted in Fig. 29(a). The angular correlation between the two final particles can be used to distinguish the ground and excited 2^+ states of the ^{10}Be fragment, as shown in Fig. 29(b). Of course, it is still difficult to see the decay to the ∼ 6 MeV states in ^{10}Be and, thus, insufficient to sort out the decay paths related to various molecular configurations, as demonstrated by experimental works using advanced silicon-strip detectors [49, 50]. The choice of the active gas as both the target material and detection medium presents another limitation.

New detection techniques have been introduced by combining the precise tracking TPC (MicroMegas type) with surrounding Si-CsI(Tl) telescope detectors, as shown in Fig. 30 [217]. This combined detector system enhances the capabilities of resonant scattering experiments by providing

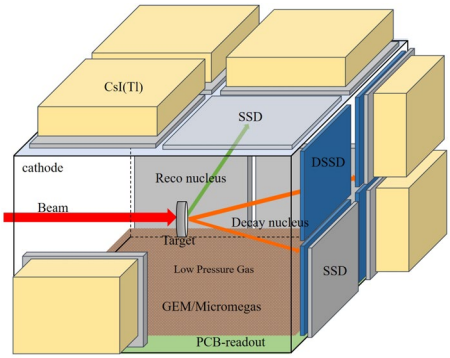

Fig. 31 (Color online) Schematic of a TPC-Si-CsI(Tl) detector with an internal solid target. The TPC is equipped with GEM/MicroMegas technology. The concept displayed in this figure was taken from Ref. [217, 220]

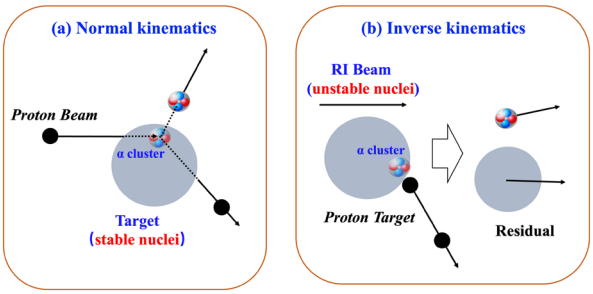

Fig. 32 (Color online) Schematic of the quasi-free (p, pα) reaction in normal **a** and inverse **b** kinematics

an improved tracking accuracy, a better energy resolution, and an excellent PID capability. A series of works have reported the use of this equipment, including the level scheme in ^{9}C [218], α clustering in ^{18}Ne [219], and various cluster configurations in ^{13}N [188].

Despite the numerous advantages of using AT-TPC in resonant scattering experiments, such as its high efficiency, tracking capability, and low detection threshold, the choice of the working gas (typically ^{4}He) remains a significant limitation. One solution might be to incorporate a thin solid target inside the TPC, as has already been realized in previous fission measurements [220], as depicted in Fig. 31. Here, the TPC plays the role of a detector, not the active target. The primary advantages would come from having a lower detection threshold and larger detection solid angle, compared with those of silicon detectors. These factors are crucial, especially for low-energy experiments.

3.4 Using knockout reactions to investigate cluster composition in nuclear ground states

According to gRDF calculations, α clusters can be formed at the low-density surface regions of heavy nuclei, but, in this case, there is a close interplay between the α-cluster formation and development of the neutron skin [62]. This interplay leads to a reduction in the neutron-skin thickness, compared with the theoretical predictions, without considering the existence of α clusters, which will further impact the experimental constraint on the density-dependence parameter L of the symmetry energy. However, the formation of α clusters is gradually hindered as the neutron skin becomes thicker. This hindrance manifests itself as a monotonic decrease in the strength of the α-cluster formation along the isotopic chain and thus can be directly examined experimentally. Hence, it is crucial to carry out new experiments to find direct experimental evidence for the existence of preformed α particles (clusters) at the surfaces of heavy nuclei and further examine the systematics of α-clustering strength along an isotopic chain into a neutron-rich region accompanied by a steady increase of the neutron skin.

When unbound, α clusters can spontaneously come out of the mother nucleus to take advantage of the quantum tunneling effect (penetration of the Coulomb barrier). This phenomenon lies at the heart of α decay from heavy nuclei and experimental studies of α-cluster structures in the excited states of light nuclei. However, α clusters are generally bound in the ground states of nuclei, particularly in neutron-rich nuclei with well-developed neutron skins, and cannot be emitted spontaneously. Therefore, to probe α clustering in these nuclei, one needs a new reaction probe that takes the α clusters out of the mother nucleus with minimized impact from the residual.

The quasi-free (p, pα) reaction is the method of choice. Figure 32(a) shows a schematic of the (p, pα) reaction in normal kinematics. Generally, a high-energy (several hundred MeV) proton beam is sent onto the target of interest. At the instant of the reaction, a certain amount of kinetic energy is transferred from the incident proton to the preformed α cluster, which gets knocked out of the target nucleus. When the transferred energy is significantly large, compared with the α separation energy, the (p, pα) reaction can be considered as quasi-free. Thus, the α cluster is knocked out without being disturbed by the residual, which can simply be considered as a spectator. Hence, the corresponding reaction cross-section provides a good measure of the strength of the preformed α cluster in the mother nucleus. Moreover, similar quasi-free nucleon knockout reactions, such as (e, ep), (p, 2p), and (p, pn) have been well-established as experimental probes to investigate the single-particle structures of nuclei [221, 222]. Furthermore, the (p, pα) reaction was widely used in the 1970s and 1980s to study the cluster structures in light stable nuclei, such as ^{9}Be and ^{12}C [223–225]. However, further extending such (p, pα) experiments into a heavier mass region was largely constrained by the then available experimental equipment and theoretical tools with which

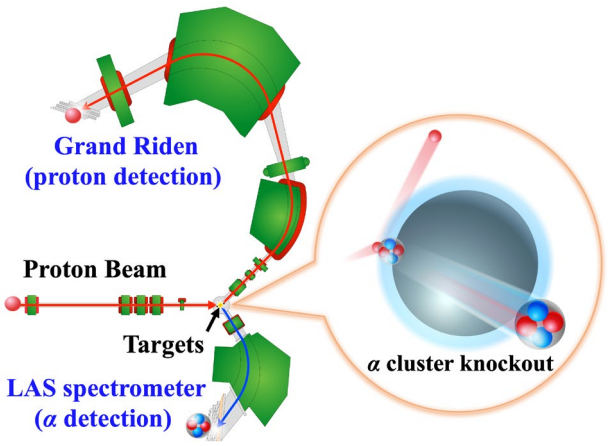

Fig. 33 (Color online) Schematic of the experimental setup of the (p, pα) reaction on heavy nuclei at RCNP. This figure was adapted from Ref. [61]

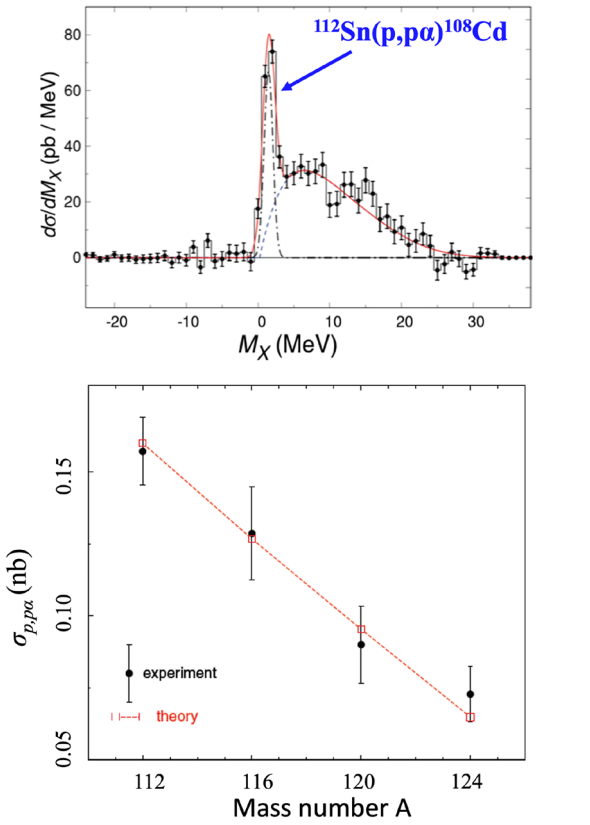

Fig. 34 (Color online) MM spectra for the α-knockout reaction ^{112}Sn (p, pα) (upper panel), and comparison of the experimental $\sigma_{p,p\alpha}$ cross-section with the theoretical prediction (lower panel). This figure was adapted from Ref. [61]

to connect the experimental results to the internal cluster structure. During the past decade, important advances have been made in both experimental techniques and theoretical tools, making the (p, pα) reaction a sensitive probe for clustering in the ground states of nuclei (e.g., Refs. [226, 227]).

In 2021, Tanaka et al. performed a quasi-free (p, pα) experiment at the Research Center for Nuclear Physics (RCNP) of Osaka University to measure the α-clustering strength and isotopic dependence of ^{112,116,120,124}Sn [61]. As illustrated in Fig. 33, the experiment was performed with the 392 MeV proton beam at the WS beam line. The scattered protons and α particles after the (p, pα) reaction were detected in coincidence using the Grand Raiden and LAS spectrometers. The experimental setup was designed according to the kinematics of the proton scattering off a preformed α particle and optimized to achieve the detection of low-energy α particles (down to ∼ 50 MeV) and a high signal-to-noise ratio. For all four tin isotopes, the MM spectrum [Fig. 34 (top panel)] shows a clear peak located at the known α-separation energy, which is simply determined by the mass, as expected for the quasi-free knockout of the preformed α clusters. Thus, these results provide direct evidence for the formation of α clusters in these tin isotopes. In addition, the observed momentum distribution of the α particles further reaffirms that the formation of the α particle indeed occurs in the low-density surface region of heavy nuclei, as predicted by theoretical calculations.

The MM spectrum is fitted using a combination of the Gaussian for the ground-state peak and the simulated line shape of the continuum background. For each tin isotope, the (p, pα) cross section $\sigma_{p,p\alpha}$ is then deduced from the integral of the ground-state peak. As shown in the bottom panel of Fig. 34, $\sigma_{p,p\alpha}$ gradually decreases as the mass number increases, with an approximately twofold decrease from ^{112}Sn to ^{124}Sn. The observed isotopic systematics of $\sigma_{p,p\alpha}$ are well-reproduced by theoretical calculations that consider the radial density distributions of the α clusters of the gRDF prediction and reaction mechanism. Further analytical results confirmed that the observed decline in $\sigma_{p,p\alpha}$ was predominantly caused by the decrease in the α-clustering strength, whereas the effect of the reaction mechanism was minor. Thus, these results support the tight interplay between the surface α-clustering and Δr_{np} in heavy nuclei and thereby lead to a reduction of Δr_{np}, in comparison to theoretical calculations that do not consider the α-clustering effect as predicted by the gRDF calculations [62]. A linear correlation between Δr_{np} and the slope parameter L has been predicted via mean-field model calculations [228] and is generally used to constrain L. Many projects worldwide are ongoing to measure the neutron skin thicknesses of heavy nuclei, such as ^{208}Pb, with sufficient precision. These results suggest the necessity of considering the effects of nuclear clustering when constraining EOS parameters from the neutron skin thickness [63].

The recent increase in the availability of secondary beams of radioactive isotopes provides new opportunities

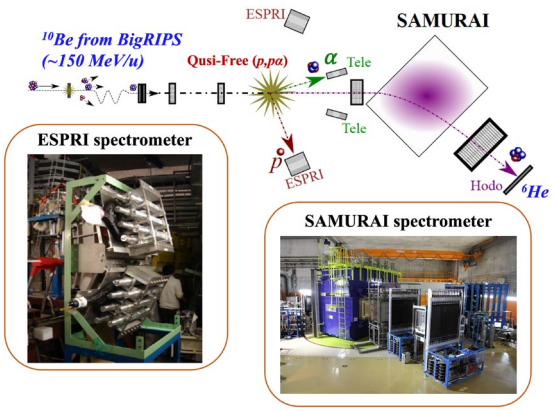

Fig. 35 (Color online) Experimental setup of the (p, pα) reaction in inverse kinematics on the neutron-rich unstable nucleus ^{10}Be at the RIBF of the RIKEN Nishina Center. This figure was adapted from Ref. [231]

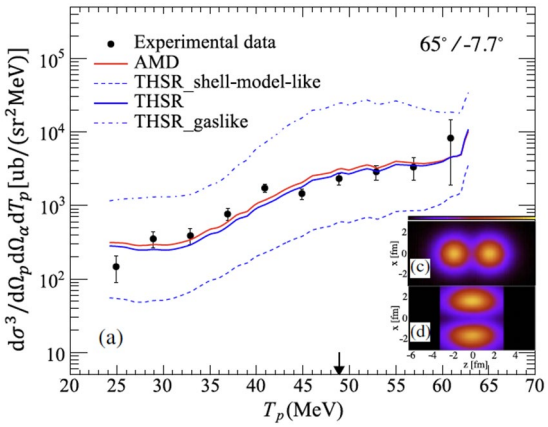

Fig. 36 (Color online) The triple differential cross-section (TDX) for ^{10}Be (p, pα) ^{6}He(g.s.), compared with theoretical calculations. The angles of the proton (θ_p) and alpha (θ_α) are chosen according to the recoilless condition of the residual. The inset shows the density distribution of the protons and valence neutrons predicted by THSR, which exhibits a well-developed α-2n-α cluster structure. This figure was adapted from Ref. [231]

to investigate α cluster structures in the ground states of unstable nuclei [17, 229, 230]. Recently, Li et al. conducted the (p, pα) reaction in inverse kinematics (Fig. 32(b)) on the neutron-rich unstable nucleus ^{10}Be [231]. A well-developed α-2n-α molecular-like cluster structure, that is, a dumbbell-like arrangement of two α cores surrounded by two valence neutrons occupying the π orbit, was predicted for the ground state of ^{10}Be by microscopic cluster models, THSR [226], and AMD [232]. The experiment was performed at the Radioactive Isotope Beam Factory (RIBF) of the RIKEN Nishina Center, and the experimental setup is illustrated in Fig. 35. From the measured angle and energy of the recoil proton and α particle, the excitation energy of the residual ^{6}He was reconstructed. This reconstruction is equivalent to the α -particle separation energy spectrum usually used in (p, pα) reactions in normal kinematics, such as [61]. In the experiment, the two reaction channels leading to different final states of the residual, namely, ^{6}He^{10}Be(p, pα)^{6}He(g.s.), ^{10}Be(p, pα)^{6}He(e.x.), were observed. Figure 36 shows that the experimental triple differential cross section (TDX) for the ^{10}Be(p, pα)^{6}He(g.s.) channel is nicely reproduced by the distorted-wave impulse approximation (DWIA) calculations that incorporate the microscopic α-cluster w.f. provided by THSR and AMD calculations. This experiment provides strong evidence for the molecular-like cluster structure of the ground state of ^{10}Be, as predicted by THSR and AMD.

4 Summary and perspectives

The nucleus is a typical quantum many-body system controlled mainly by short-range nuclear forces. This system, having neither a concrete center nor a confinement boundary, may exhibit large structural flexibility, including the overall shape changes and formation of the internal substructure, such as clusters. When moving toward the driplines or getting excited toward some cluster separation thresholds, small or even negative binding energy, corresponding to a relatively weak overall interaction, favors the local correlation and cluster formation [3, 4, 23, 233, 234]. Furthermore, the antisymmetrization among nucleons (Pauli blocking effect) tends to stabilize the cluster separation around the threshold energy, and the orthogonality between the quantum states drives the system to more intriguing exotic structure configurations. Cluster structures also play important roles in nuclear astrophysics processes, such as the synthesis of elements via fusion reactions, which are sensitive to cluster resonant states that are close to the threshold [19, 20]. Attention was also attracted to the inclusion of nuclear structure effects, such as deformation and clustering, into heavy-ion collision processes at intermediate and relativistic energies [235, 236].

The idea of RGM, introduced by Wheeler [12], provides a reasonable working base to address the flexibility of the nuclear structure. It is particularly useful to describe the mixing of the single-particle and clustering configurations by applying different representations to different groups of nucleons, as already realized in many instances (e.g. Ref. [59]). The main difficulties here involve the complexity of real calculations, although some simplification methods have been developed for certain cases, such as combining RGM with GCM or OCM. Moreover, RGM + GCM or RGM + OCM calculations can be applied to scattering (reaction)

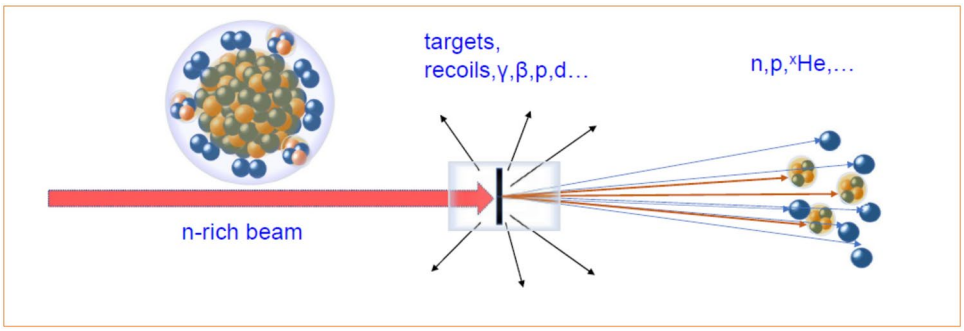

Fig. 37 (Color online) Anticipated future detection requirements when using a heavy neutron-rich beam, including the precise multi-neutron and multi-fragment detection at forward angles and the novel target system equipped with recoil particle detectors

process as long as the c.m. coordinates are extended to large values ([237] and the references cited therein). The reaction theory is generally much less developed, compared with the structure theory, when multi-nucleon (cluster) correlation effects are encountered. Considering the increasing interest in applying multi-nucleon transfer (MNT) reactions to produce heavy neutron-rich nuclei and subsequently executing fission or neutron-evaporation processes [238–240], the RGM-type reaction models may need to be developed via the invention of appropriate approximation methods. Owing to the importance of antisymmetrization in forming the cluster structure and shaping the reaction processes, it is challenging to maintain this antisymmetry throughout the MNT calculations. The application of AMD-type approaches to heavy systems might present a promising solution. Because the local nucleon correlation is sensitive to the specific nuclear force, the cluster structure can serve as a testing ground for *ab initio*-type nuclear forces rooted in quantum chromodynamics (QCD) [17, 241]. Considering the complexity of the anticipated problems, artificial intelligence (AI) and machine learning should be of great help when implementing the theoretical solutions.

This review demonstrates the advantages of using the Brink-type wave-packet presentation to describe clustering phenomena. The orbital (eigenstate of the angular momentum) presentation favors the description of the independent-particle motion in a centralized average potential, making it easier to reproduce the shell-like structure, including the magic numbers. However, it is difficult to address the strong multi-nucleon correlations unless an infinitely large model space is used. In contrast, the wave packet presentation may directly capture the local correlation instead of the orbital behavior. When moving to heavy neutron-rich systems, as can be expected with the future RIB facilities, the structure may reasonably become a shell-like core plus an expanded clustering surface, as depicted by the inset image in the bottom-right corner of Fig. 1. The flexible combination of both presentation modes under the RGM framework will likely be a key point in future theoretical approaches.

In addition to the investigation of the cluster structure around the separation thresholds via the aforementioned MM or IM methods, cluster structures in the nuclear ground states have recently become another focus of research. Leveraging the operating and upcoming RIB facilities worldwide, such as RIBF (Japan), FRIB (US), GSI/FAIR (Germany), HIAF (China) and RAON (South Korea), cluster knockout experiments, such as (p, pα), will be applied to more neutron-rich nuclei to probe cluster structures in their ground states. Theoretical calculations predicted that the formation of clusters could be favored in the ground state of light, neutron-rich nuclei, such as beryllium and carbon isotopes [17, 229, 230]. Neutron-rich nuclei with novel mixed states of clusters and neutrons could also serve as unique settings for investigations regarding the properties of neutron-rich matter, particularly when considering inhomogeneity due to the formation of clusters. Dedicated detector systems, such as TOGAXSI at RIBF of the RIKEN Nishna Center, are currently under development for the (p, pα) reaction in inverse kinematics on unstable nuclei [242]. It would also be interesting to investigate the formation of other light clusters, such as deuterons, tritons, and ^{3}He, by using similar quasi-free knockout reactions, which are predicted to behave similarly to α clusters [63, 243–245].

Experimentally, combining the knockout reaction method at high energies and the excitation decay IM method at lower energies would still be necessary to probe different aspects of nuclear clustering. The former is applicable to the ground and low-lying states of the nucleus, whereas the latter is able to touch many more thresholds where new, exotic cluster configurations may emerge. Because neutron coupling and multi-neutron emissions will be essential in future experiments for investigating heavy, neutron-rich systems, relevant detection systems should be developed to simultaneously record multi-fragments and multi-neutrons (Fig. 37), although these tasks will be challenging.

References

1. R. Genzel, F. Eisenhauer, S. Gillessen, The galactic center massive black hole and nuclear star cluster. Rev. Mod. Phys. **82**, 3121–3195 (2010). https://doi.org/10.1103/RevModPhys.82.3121
2. H.X. Chen, W. Chen, X. Liu et al., The hidden-charm pentaquark and tetraquark states. Phys. Rep. **639**, 1–121 (2016). https://doi.org/10.1016/j.physrep.2016.05.004
3. W. von Oertzen, M. Freer, Y. Kanada-En'yo, Nuclear clusters and nuclear molecules. Phys. Rep. **432**, 43–113 (2006). https://doi.org/10.1016/j.physrep.2006.07.001
4. Y. Ye, X. Yang, H. Sakurai et al., Physics of exotic nuclei. Nat. Rev. Phys. (2024)
5. F. Kondev, M. Wang, W. Huang et al., The NUBASE2020 evaluation of nuclear physics properties*. Chin. Phys. C **45**, 030001 (2021). https://doi.org/10.1088/1674-1137/abddae
6. H. Koura, T. Tachibana, M. Uno et al., Nuclidic mass formula on a spherical basis with an improved even-odd term. Prog. Theor. Phys. **113**, 305 (2005). https://doi.org/10.1143/PTP.113.305
7. K. Heyde, *Basic Ideas and Concepts in Nuclear Physics*, (IOP Publishing Ltd, Dirac House, Temple Back, Bristol BS1 6BE, UK, 2004)
8. G. Gamow, *Constitution of Atomic Nuclei and Radioactivity*, (Oxford University Press, Great Clarendon Street Oxford OX2 6DP, 1931)
9. D.M. Brink, History of cluster structure in nuclei. J. Phys. Conf. Ser. **111**, 012001 (2008). https://doi.org/10.1088/1742-6596/111/1/012001
10. H.A. Bethe, R.F. Bacher, Nuclear physics A. stationary states of nuclei. Rev. Mod. Phys. **8**, 82–229 (1936). https://doi.org/10.1103/RevModPhys.8.82
11. L. Hafstad, The alpha-particle model of the nucleus. Phys. Rev. **54**, 681–692 (1938). https://doi.org/10.1103/PhysRev.54.681
12. J.A. Wheeler, On the mathematical description of light nuclei by the method of resonating group structure. Phys. Rev. **52**, 1107–1122 (1937). https://doi.org/10.1103/PhysRev.52.1107
13. J.J. Griffin, J.A. Wheeler, Collective motions in nuclei by the method of generator coordinates. Phys. Rev. **108**, 311–327 (1957). https://doi.org/10.1103/PhysRev.108.311
14. S. Saito, Effect of Pauli principle in scattering of two clusters. Prog. Theo. Phys. **40**, 893–894 (1968). https://doi.org/10.1143/PTP.40.893
15. Y. Funaki, H. Horiuchi, A. Tohsaki, Cluster models from RGM to alpha condensation and beyond. Prog. Part. Nucl. Phys. **82**, 78–132 (2015). https://doi.org/10.1016/j.ppnp.2015.01.001
16. A. Tohsaki, H. Horiuchi, P. Schuck et al., Colloquium: status of α-particle condensate structure of the hoyle state. Rev. Mod. Phys. **89**, 011002 (2017). https://doi.org/10.1103/RevModPhys.89.011002
17. M. Freer, H. Horiuchi, Y. Kanada-En'yo et al., Microscopic clustering in light nuclei. Rev. Mod. Phys. **90**, 035004 (2018). https://doi.org/10.1103/RevModPhys.90.035004
18. F.S. Hoyle, On nuclear reactions occurring in very hot stars. I. The synthesis of elements from carbon to nickel. Astrophys. J. Suppl. S. **1**, 121–146 (1954). https://doi.org/10.1086/190005
19. M. Freer, H. Fynbo, The Hoyle state in ^{12}C. Prog. Part. Nucl. Phys. **78**, 1–23 (2014). https://doi.org/10.1016/j.ppnp.2014.06.001
20. S. Kubono, D.N. Binh, S. Hayakawa et al., Nuclear clusters in astrophysics. Nucl. Phys. A **834**, 647c–650c (2010). https://doi.org/10.1016/j.nuclphysa.2010.01.113
21. H. Horiuchi, K. Ikeda, A molecule-like structure in atomic nuclei of ^{16}O* and ^{20}Ne*. Prog. Theor. Phys. **40**, 277 (1968). https://doi.org/10.1143/PTP.40.277
22. D. Brink, Alpha cluster model. Proceedings of the International School of Physics Enrico Fermi, Varenna Course 36 (Academic Press, New York) p. 247 (1966)
23. K. Ikeda, N. Takigawa, H. Horiuchi, The systematic structure-change into the molecule-like structures in the self-conjugate 4n nuclei. Prog. Theor. Phys. Suppl. E **68**, 464–475 (1968). https://doi.org/10.1143/PTPS.E68.464
24. G. Röpke, A. Schnell, P. Schuck et al., Four-particle condensate in strongly coupled fermion systems. Phys. Rev. Lett. **80**, 3177–3180 (1998). https://doi.org/10.1103/PhysRevLett.80.3177
25. A. Tohsaki, H. Horiuchi, P. Schuck et al., Alpha cluster condensation in ^{12}C and ^{16}O. Phys. Rev. Lett. **87**, 192501 (2001). https://doi.org/10.1103/PhysRevLett.87.192501
26. Y. Funaki, H. Horiuchi, W. von Oertzen et al., Concepts of nuclear α-particle condensation. Phys. Rev. C **80**, 064326 (2009). https://doi.org/10.1103/PhysRevC.80.064326
27. B. Zhou, Y. Funaki, H. Horiuchi et al., The 5α condensate state in ^{20}Ne. Nat. Commun. **14**, 8206 (2023). https://doi.org/10.1038/s41467-023-43816-9
28. J.H. Chen, Y.L. Ye, K. Ma et al., New evidence of the hoyle-like structure in ^{16}O. Sci. Bull. **68**, 1119–1126 (2023). https://doi.org/10.1016/j.scib.2023.04.031
29. S. Okabe, Y. Abe, H. Tanaka, The structure of ^{9}Be nucleus by a molecular model. I). Prog. Theor. Phys. **57**, 866–881 (1977). https://doi.org/10.1143/PTP.57.866
30. S. Okabe, Y. Abe, The structure of ^{9}Be by a molecular. II. Prog. Theor. Phys. **61**, 1049–1064 (1979). https://doi.org/10.1143/PTP.61.1049
31. Y. Liu, Y.L. Ye, Nuclear clustering in light neutron-rich nuclei. Nucl. Sci. Tech. **29**, 184 (2018). https://doi.org/10.1007/s41365-018-0522-x
32. Y. Kanada-En'yo, H. Horiuchi, A. Ono, Structure of Li and Be isotopes studied with antisymmetrized molecular dynamics. Phys. Rev. C **52**, 628 (1995). https://doi.org/10.1103/PhysRevC.52.628-646
33. Y. Kanada-En'yo, M. Kimura, A. Ono, Antisymmetrized molecular dynamics and its applications to cluster phenomena. Prog. Theor. Exp. Phys. **2012**, 01A202 (2012). https://doi.org/10.1093/ptep/pts001
34. H. Feldmeier, Fermionic molecular dynamics. Nucl. Phys. A **515**, 147–172 (1990). https://doi.org/10.1016/0375-9474(90)90328-J
35. Q. Zhao, M. Lyu, Z.Z. Ren et al., Contact representation of short-range correlation in light nuclei studied by the high-momentum antisymmetrized molecular dynamics. Phys. Rev. C **99**, 034311 (2019). https://doi.org/10.1103/PhysRevC.99.034311
36. B. Zhou, Y. Funaki, A. Tohsaki et al., The container picture with two-alpha correlation for the ground state of ^{12}C. Prog. Theor. Exp. Phys. **2014**, 101D01 (2014). https://doi.org/10.1093/ptep/ptu127
37. B. Zhou, Y. Funaki, H. Horiuchi et al., Nonlocalized clustering: a new concept in nuclear cluster structure physics. Phys. Rev. Lett. **110**, 262501 (2013). https://doi.org/10.1103/PhysRevLett.110.262501
38. Y. Funaki, "Container'' evolution for cluster structures in ^{16}O. Phys. Rev. C **97**, 021304 (2018). https://doi.org/10.1103/PhysRevC.97.021304

39. N. Itagaki, S. Okabe, Molecular orbital structures in ^{10}Be. Phys. Rev. C **61**, 044306 (2000). https://doi.org/10.1103/PhysRevC.61.044306
40. M. Ito, N. Itagaki, H. Sakurai et al., Coexistence of covalent superdeformation and molecular resonances in an unbound region of ^{12}Be. Phys. Rev. Lett. **100**, 182501 (2008). https://doi.org/10.1103/PhysRevLett.100.182502
41. P.W. Zhao, N. Itagaki, J. Meng, Rod-shaped nuclei at extreme spin and isospin. Phys. Rev. Lett. **115**, 022501 (2015). https://doi.org/10.1103/PhysRevLett.115.022501
42. T. Otsuka, T. Abe, T. Yoshida et al., α-clustering in atomic nuclei from first principles with statistical learning and the hoyle state character. Nat. Commun. **13**, 2234 (2022). https://doi.org/10.1038/s41467-022-29582-0
43. W.B. He, Y.G. Ma, X.G. Cao et al., Giant dipole resonance as a fingerprint of α clustering configurations in ^{12}C and ^{16}O. Phys. Rev. Lett. **113**, 032506 (2014). https://doi.org/10.1103/PhysRevLett.113.032506
44. M. Freer, E. Casarejos, L. Achouri et al., α: 2n: α molecular band in ^{10}Be. Phys. Rev. Lett. **96**, 042501 (2006). https://doi.org/10.1103/PhysRevLett.96.042501
45. W. Jiang, Y.L. Ye, C.J. Lin et al., Determination of the cluster-decay branching ratio from a near-threshold molecular state in ^{10}Be. Phys. Rev. C **101**, 031304(R) (2020). https://doi.org/10.1103/PhysRevC.101.031304
46. Z.H. Yang, Y.L. Ye, Z.H. Li et al., Observation of enhanced monopole strength and clustering in ^{12}Be. Phys. Rev. Lett. **112**, 162501 (2014). https://doi.org/10.1103/PhysRevLett.112.162501
47. H. Yamaguchi, D. Kahl, S. Hayakawa et al., Experimental investigation of a linear-chain structure in the nucleus ^{14}C. Phys. Lett. B **766**, 11–16 (2017). https://doi.org/10.1016/j.physletb.2016.12.050
48. J. Li, Y.L. Ye, Z.H. Li et al., Selective decay from a candidate of the σ-bond linear-chain state in ^{14}C. Phys. Rev. C **95**, 021303(R) (2017). https://doi.org/10.1103/PhysRevC.95.021303
49. Y. Liu, Y.L. Ye, J.L. Lou et al., Positive-parity linear-chain molecular band in ^{16}C. Phys. Rev. Lett. **124**, 192501 (2020). https://doi.org/10.1103/PhysRevLett.124.192501
50. J.X. Han, Y.L. Ye, J.L. Lou et al., Nuclear linear-chain structure arises in carbon-14. Commun. Phys. **6**, 220 (2023). https://doi.org/10.1038/s42005-023-01342-6
51. H. Morinaga, Interpretation of some of the excited states of 4n self-conjugate nuclei. Phys. Rev. **101**, 254 (1956). https://doi.org/10.1103/PhysRev.101.254
52. P.G. Hansen, B. Jonson, The neutron halo of extremely neutron-rich nuclei. Europhys. Lett. **4**, 409 (1987). https://doi.org/10.1209/0295-5075/4/4/005
53. M. Zhukov, B. Danilin, D. Fedorov et al., Bound state properties of Borromean halo nuclei: ^{6}He and ^{11}Li. Phys. Rep. **231**, 151–199 (1993). https://doi.org/10.1016/0370-1573(93)90141-Y
54. M. Matsuo, Spatial structure of neutron cooper pair in low density uniform matter. Phys. Rev. C **73**, 044309 (2006). https://doi.org/10.1103/PhysRevC.73.044309
55. K. Hagino, H. Sagawa, J. Carbonell et al., Coexistence of BCS- and BEC-like pair structures in halo nuclei. Phys. Rev. Lett. **99**, 022506 (2007). https://doi.org/10.1103/PhysRevLett.99.022506
56. L.V. Grigorenko, J.S. Vaagen, M.V. Zhukov, Exploring the manifestation and nature of a dineutron in two-neutron emission using a dynamical dineutron model. Phys. Rev. C **97**, 034605 (2018). https://doi.org/10.1103/PhysRevC.97.034605
57. S.M. Wang, W. Nazarewicz, Fermion pair dynamics in open quantum systems. Phys. Rev. Lett. **126**, 142501 (2021). https://doi.org/10.1103/PhysRevLett.126.142501
58. Y. Kubota, A. Corsi, G. Authelet et al., Surface localization of the dineutron in ^{11}Li. Phys. Rev. Lett. **125**, 252501 (2020). https://doi.org/10.1103/PhysRevPhysRevLett.125.252501
59. F. Kobayashi, Y. Kanada-En'yo, Dineutron formation and breaking in ^{8}He. Phys. Rev. C **88**, 034321 (2013). https://doi.org/10.1103/PhysRevC.88.034321
60. Z.H. Yang, Y.L. Ye, B. Zhou et al., Observation of the exotic 0_2^+ cluster state in ^{8}He. Phys. Rev. Lett. **131**, 242501 (2023). https://doi.org/10.1103/PhysRevPhysRevLett.131.242501
61. J. Tanaka, Z. Yang, S. Typel et al., Formation of clusters in dilute neutron-rich matter. Science **371**, 260–264 (2021). https://doi.org/10.1126/science.abe4688
62. S. Typel, Neutron skin thickness of heavy nuclei with α-particle correlations and the slope of the nuclear symmetry energy. Phys. Rev. C **89**, 064321 (2014). https://doi.org/10.1103/PhysRevC.89.064321
63. M. Oertel, M. Hempel, T. Klähn et al., Equations of state for supernovae and compact stars. Rev. Mod. Phys. **89**, 015007 (2017). https://doi.org/10.1103/RevModPhys.89.015007
64. Z. Yang, S. Huang, Clustering in nuclear systems: from finite nuclei to neutron stars. Sci. Bull. **66**, 2054–2056 (2021). https://doi.org/10.1016/j.scib.2021.07.009
65. T. Baba, M. Kimura, Three-body decay of linear-chain states in ^{14}C. Phys. Rev. C **95**, 064318 (2017). https://doi.org/10.1103/PhysRevC.95.064318
66. T. Baba, M. Kimura, Characteristic α and ^{6}He decays of linear-chain structures in ^{16}C. Phys. Rev. C **97**, 054315 (2018). https://doi.org/10.1103/PhysRevC.97.054315
67. S. Saito, Chapter II. Theory of resonating group method and generator coordinate method, and orthogonality condition model. Prog. Theor. Phys. Suppl. **62**, 11–89 (1977). https://doi.org/10.1143/PTPS.62.11
68. W.E. Hunt, M.K. Mehta, R.H. Davis, Scattering of alpha particles by oxygen. I. Bombarding energy range 5.8 to 10.0 MeV. Phys. Rev. **160**, 782–790 (1967). https://doi.org/10.1103/PhysRev.160.782
69. Y.C. Tang, M. LeMere, D.R. Thompsom, Resonating-group method for nuclear many-body problems. Phys. Rep. **47**, 167–223 (1978). https://doi.org/10.1016/0370-1573(78)90175-8
70. K. Fujimura, D. Baye, P. Descouvemont et al., Low-energy α+^{6}He elastic scattering with the resonating-group method. Phys. Rev. C **59**, 817–825 (1999). https://doi.org/10.1103/PhysRevC.59.817
71. H. Horiuchi, Generator coordinate treatment of composite particle reaction and molecule-like structures. Prog. Theor. Phys. **43**, 375–389 (1970). https://doi.org/10.1143/PTP.43.375
72. T. Myo, H. Takemoto, Resonances and scattering in microscopic cluster models with the complex-scaled generator coordinate method. Phys. Rev. C **107**, 064308 (2023). https://doi.org/10.1103/PhysRevC.107.064308
73. D. Baye, P. Descouvemont, F. Leo, Microscopic cluster model analysis of ^{14}O+p elastic scattering. Phys. Rev. C **72**, 024309 (2005). https://doi.org/10.1103/PhysRevC.72.024309
74. V.K. Lukyanov, D.N. Kadrev, E.V. Zemlyanaya et al., Microscopic analysis of ^{10,11}Be elastic scattering on protons and nuclei, and breakup processes of ^{11}Be within the ^{10}Be+n cluster model. Phys. Rev. C **91**, 034606 (2015). https://doi.org/10.1103/PhysRevC.91.034606
75. B. Zhou, M. Kimura, 2α + t cluster structure in ^{11}B. Phys. Rev. C **98**, 054323 (2018). https://doi.org/10.1103/PhysRevC.98.054323
76. T. Matsuse, M. Kamimura, A study of α-widths of ^{20}Ne based on ^{16}O and α-cluster model. Prog. Theor. Phys. **49**, 1765–1767 (1973). https://doi.org/10.1143/PTP.49.1765

77. H. Horiuchi, Many-cluster problem by the orthogonality condition model: general discussion and ^{12}C problem. Prog. Theor. Phys. **53**, 447–460 (1975). https://doi.org/10.1143/PTP.53.447
78. T. Yamada, Y. Funaki, α-cluster structures and monopole excitations in ^{13}C. Phys. Rev. C **92**, 034326 (2015). https://doi.org/10.1103/PhysRevC.92.034326
79. J. Feng, Y.L. Ye, B. Yang et al., Enhanced monopole transition strength from the cluster-decay of ^{13}C. Sci. China Phys. Mech. Astron. **62**, 1–7 (2019). https://doi.org/10.1007/s11433-018-9258-7
80. Q. Wu, Y. Funaki, X. Chen, Cluster structures of the 0^+ states of $^{13}_{\Lambda}$C with the $3\alpha + \Lambda$ four-body orthogonality condition model. Phys. Rev. C **107**, 014317 (2023). https://doi.org/10.1103/PhysRevC.107.014317
81. T. Yamada, Y. Funaki, $\alpha + \alpha + t$ cluster structures and ^{12}C(0^+_2) -analog states in ^{11}B. Phys. Rev. C **82**, 064315 (2010). https://doi.org/10.1103/PhysRevC.82.064315
82. J. Wheeler, Molecular viewpoints in nuclear structure. Phys. Rev. **52**, 1083 (1937). https://doi.org/10.1103/PhysRev.52.1083
83. Y. Abe, J. Hiura, H. Tanaka, On the Stability of α-Cluster Structures in ^{8}Be and ^{12}C Nuclei. Prog. Theor. Phys. **46**, 352–354 (1971). https://doi.org/10.1143/PTP.46.352
84. H. Horiuchi, K. Ikeda, K. Katō, Recent developments in nuclear cluster physics. Prog. Theor. Phys. Suppl. **192**, 1–238 (2012). https://doi.org/10.1143/PTPS.192.1
85. Y. Abe, J. Hiura, H. Tanaka, A molecular-obital model of the atomic nuclei. Prog. Theor. Phys. **49**, 800–824 (1973). https://doi.org/10.1143/PTP.49.800
86. W. von Oertzen, Two-center molecular states in ^{9}B, ^{9}Be, ^{10}Be, and ^{10}B. Z. Phys. A **354**, 37–43 (1996). https://doi.org/10.1007/s002180050010
87. N. Itagaki, S. Okabe, K. Ikeda et al., Molecular-orbital structure in neutron-rich C isotopes. Phys. Rev. C **64**, 014301 (2001). https://doi.org/10.1103/PhysRevC.64.014301
88. M. Ito, K. Kato, K. Ikeda, Application of the generalized two-center cluster model to ^{10}Be. Phys. Lett. B **588**, 43–48 (2004). https://doi.org/10.1016/j.physletb.2004.01.090
89. M. Ito, K. Ileda, Unified studies of chemical bonding structures and resonant scattering in light neutron-excess systems, ^{10,12}Be. Rep. Prog. Phys. **77**, 096301 (2014). https://doi.org/10.1088/0034-4885/77/9/096301
90. M. Ito, Imprint of adiabatic structures in monopole excitations of ^{12}Be. Phys. Rev. C **83**, 044319 (2011). https://doi.org/10.1103/PhysRevC.83.044319
91. A. Ono, H. Horiuchi, T. Maruyama et al., Fragment formation studied with antisymmetrized version of molecular dynamics with two-nucleon collisions. Phys. Rev. Lett. **68**, 2898–2900 (1992). https://doi.org/10.1103/PhysRevLett.68.2898
92. M. Chernykh, H. Feldmeier, T. Neff et al., Structure of the hoyle state in ^{12}C. Phys. Rev. Lett. **98**, 032501 (2007). https://doi.org/10.1103/PhysRevLett.98.032501
93. T. Neff, H. Feldmeier, Cluster structures within fermionic molecular dynamics. Nucl. Phys. A **738**, 357–361 (2004). https://doi.org/10.1016/j.nuclphysa.2004.04.061
94. Y. Kanada-En'yo, Dineutron structure in ^{8}He. Phys. Rev. C **76**, 044323 (2007). https://doi.org/10.1103/PhysRevC.76.044323
95. T. Ando, K. Ikeda, A. Tohsaki-Suzuki, Nucleus–nucleus interaction and nuclear saturation property: microscopic study of ^{16}O+^{16}O interaction by new effective nuclear force. Prog. Theor. Phys. **64**, 1608–1626 (1980). https://doi.org/10.1143/PTP.64.1608
96. J. Dechargé, D. Gogny, Hartree–Fock–Bogolyubov calculations with the $D1$ effective interaction on spherical nuclei. Phys. Rev. C **21**, 1568–1593 (1980). https://doi.org/10.1103/PhysRevC.21.1568
97. Y. Kanada-En'yo, Variation after angular momentum projection for the study of excited states based on antisymmetrized molecular dynamics. Phys. Rev. Lett. **81**, 5291–5293 (1998). https://doi.org/10.1103/PhysRevLett.81.5291
98. Y. Kanada-En'yo, H. Horiuchi, A. Doté, Structure of excited states of ^{10}Be studied with antisymmetrized molecular dynamics. Phys. Rev. C **60**, 064304 (1999). https://doi.org/10.1103/PhysRevC.60.064304
99. T. Baba, M. Kimura, Structure and decay pattern of the linear-chain state in ^{14}C. Phys. Rev. C **94**, 044303 (2016). https://doi.org/10.1103/PhysRevC.94.044303
100. T. Baba, M. Kimura, Coulomb shift in the mirror pair of ^{14}C and ^{14}O as a signature of the linear-chain structure. Phys. Rev. C **99**, 021303 (2019). https://doi.org/10.1103/PhysRevC.99.021303
101. T. Baba, Y. Liu, J.X. Han et al., Pure σ-bond linear chain in ^{16}C. Phys. Rev. C **102**, 041302 (2020). https://doi.org/10.1103/PhysRevC.102.041302
102. M. Freer, J.D. Malcolm, N.L. Achouri et al., Resonances in ^{14}C observed in the ^{4}He(^{10}Be,α)^{10}Be reaction. Phys. Rev. C **90**, 054324 (2014). https://doi.org/10.1103/PhysRevC.90.054324
103. A. Fritsch, S. Beceiro-Novo, D. Suzuki et al., One-dimensionality in atomic nuclei: a candidate for linear-chain α clustering in ^{14}C. Phys. Rev. C **93**, 014321 (2016). https://doi.org/10.1103/PhysRevC.93.014321
104. J.B. Ehrman, On the displacement of corresponding energy levels of ^{13}C and ^{13}N. Phys. Rev. **81**, 412–416 (1951). https://doi.org/10.1103/PhysRev.81.412
105. R.G. Thomas, An analysis of the energy levels of the mirror nuclei, ^{13}C and ^{13}N. Phys. Rev. **88**, 1109–1125 (1952). https://doi.org/10.1103/PhysRev.88.1109
106. Y.H. Yang, Y.G. Ma, S.M. Wang et al., Structure and decay mechanism of the low-lying states in ^{9}Be and ^{9}B. Phys. Rev. C **108**, 044307 (2023). https://doi.org/10.1103/PhysRevC.108.044307
107. Y. Funaki, A. Tohsaki, H. Horiuchi et al., Analysis of previous microscopic calculations for the second 0^+ state in ^{12}C in terms of 3-α particle bose-condensed state. Phys. Rev. C **67**, 051306R (2003). https://doi.org/10.1103/PhysRevC.67.051306
108. Y. Funaki, H. Horiuchi, A. Tohsaki et al., Description of ^{8}Be as deformed gas-like two-alpha-particle states. Prog. Theor. Phys. **108**, 297–322 (2002). https://doi.org/10.1143/PTP.108.297
109. B. Zhou, Y. Funaki, H. Horiuchi et al., Nonlocalized cluster dynamics and nuclear molecular structure. Phys. Rev. C **89**, 034319 (2014). https://doi.org/10.1103/PhysRevC.89.034319
110. B. Zhou, Z.Z. Ren, C. Xu et al., New concept for the ground-state band in ^{20}Ne within a microscopic cluster model. Phys. Rev. C **86**, 014301 (2012). https://doi.org/10.1103/PhysRevC.86.014301
111. S. Adachi, Y. Fujikawa, T. Kawabata et al., Candidates for the 5α condensed state in ^{20}Ne. Phys. Lett. B **819**, 136411 (2021). https://doi.org/10.1016/j.physletb.2021.136411
112. G. Gamow, Zur quantentheorie des atomkernes. Z. Phys. **51**, 204–212 (1928). https://doi.org/10.1007/BF01343196
113. G. Gamow, Mass defect curve and nuclear constitution. Proc. Roy. Soc. A **126**, 632 (1930). https://doi.org/10.1098/rspa.1930.0032
114. I. Tonozuka, A. Arima, Surface -clustering and -decays of ^{212}Po. Nucl. Phys. A **323**, 45–60 (1979). https://doi.org/10.1016/0375-9474(79)90415-9
115. K. Varga, R.G. Lovas, R.J. Liotta, Absolute alpha decay width of ^{212}Po in a combined shell and cluster model. Phys. Rev. Lett. **69**, 37–40 (1992). https://doi.org/10.1103/PhysRevLett.69.37
116. C. Qi, A.N. Andreyev, M. Huyse et al., Abrupt changes in α-decay systematics as a manifestation of collective nuclear modes.

Phys. Rev. C **81**, 064319 (2010). https://doi.org/10.1103/PhysRevC.81.064319
117. D. Delion, A. Insolia, R. Liotta, Photon–neutron correlations and microscopic description of alpha decay. Nucl. Phys. A **549**, 407–419 (1992). https://doi.org/10.1016/0375-9474(92)90087-Z
118. R.I. Betan, W. Nazarewicz, α decay in the complex-energy shell model. Phys. Rev. C **86**, 034338 (2012). https://doi.org/10.1103/PhysRevC.86.034338
119. C. Xu, Z.Z. Ren, Global calculation of α-decay half-lives with a deformed density-dependent cluster model. Phys. Rev. C **74**, 014304 (2006). https://doi.org/10.1103/PhysRevC.74.014304
120. D.S. Delion, R.J. Liotta, R. Wyss, Exact estimate of the α-decay rate and semiclassical approach in deformed nuclei. Phys. Rev. C **92**, 051301 (2015). https://doi.org/10.1103/PhysRevC.92.051301
121. S. Yang, C. Xu, G. Röpke, α-cluster formation and decay: the role of shell structure. Phys. Rev. C **104**, 034302 (2021). https://doi.org/10.1103/PhysRevC.104.034302
122. J. Dong, Q. Zhao, W. Wang, L.J. Zuo et al., α-cluster formation in heavy-emitters within a multistep model. Phys. Lett. B **813**, 136063 (2021). https://doi.org/10.1016/j.physletb.2021.136063
123. Y. Qian, Z. Ren, New insight into α clustering of heavy nuclei via their α decay. Phys. Lett. B **777**, 298–302 (2018). https://doi.org/10.1016/j.physletb.2017.12.046
124. C. Xu, Z.Z. Ren, G. Röpke et al., α-decay width of ^{212}Po from a quartetting wave function approach. Phys. Rev. C **93**, 011306 (2016). https://doi.org/10.1103/PhysRevC.93.011306
125. J.G. Deng, H.F. Zhang, G. Royer, Improved empirical formula for α-decay half-lives. Phys. Rev. C **101**, 034307 (2020). https://doi.org/10.1103/PhysRevC.101.034307
126. D. Ward, B. Carlsson, S. Aberg, Alpha-particle formation and decay rates from skyrme-HFB wave functions. Phys. Scr. **89**, 054027 (2014). https://doi.org/10.1088/0031-8949/89/5/054027
127. S.L. Tang, Y.B. Qian, Z.Z. Ren, Model-independent analysis on the regular behavior of α preformation probability in heavy nuclei. Phys. Rev. C **108**, 064303 (2023). https://doi.org/10.1103/PhysRevC.108.064303
128. J.G. Deng, H.F. Zhang, Analytic formula for estimating the α -particle preformation factor. Phys. Rev. C **102**, 044314 (2020). https://doi.org/10.1103/PhysRevC.102.044314
129. K. Wei, H.F. Zhang, α decay and cluster radioactivity within the redefined preformed cluster method. Phys. Rev. C **102**, 034318 (2020). https://doi.org/10.1103/PhysRevC.102.034318
130. Y.Z. Wang, J.Z. Gu, Z.Y. Hou, Preformation factor for α particles in isotopes near $N = Z$. Phys. Rev. C **89**, 047301 (2014). https://doi.org/10.1103/PhysRevC.89.047301
131. G. Röpke, P. Schuck, Y. Funaki et al., Nuclear clusters bound to doubly magic nuclei: the case of ^{212}Po. Phys. Rev. C **90**, 034304 (2014). https://doi.org/10.1103/PhysRevC.90.034304
132. G. Röpke, P. Schuck, C. Xu et al., Alpha-like clustering in ^{20}Ne from a quartetting wave function approach. J. Low Temp. Phys. **189**, 383–409 (2017). https://doi.org/10.1007/s10909-017-1796-9
133. C. Xu, G. Röpke, P. Schuck et al., α-cluster formation and decay in the quartetting wave function approach. Phys. Rev. C **95**, 061306 (2017). https://doi.org/10.1103/PhysRevC.95.061306
134. S. Yang, C. Xu, G. Röpke et al., α decay to a doubly magic core in the quartetting wave function approach. Phys. Rev. C **101**, 024316 (2020). https://doi.org/10.1103/PhysRevC.101.024316
135. S.A. Gurvitz, G. Kalbermann, Decay width and the shift of a quasistationary state. Phys. Rev. Lett. **59**, 262–265 (1987). https://doi.org/10.1103/PhysRevLett.59.262
136. S.A. Gurvitz, Novel approach to tunneling problems. Phys. Rev. A **38**, 1747–1759 (1988). https://doi.org/10.1103/PhysRevA.38.1747
137. C.A. Bertulani, P. Danielewicz, Introduction to Nuclear Reactions, (IOP Publishing Ltd, Dirac House, Temple Back, Bristol BS1 6BE, UK, 2004)
138. W. von Oertzen, H. Bohlen, M. Milin et al., Search for cluster structure of excited states in ^{14}C. Eur. Phys. J. A **21**, 193–215 (2004). https://doi.org/10.1140/epja/i2003-10188-9
139. H. Bohlen, W. von Oertzen, M. Milin et al., Structures in ^{20}O from the ^{14}C(^{7}Li, p) reaction at 44 MeV. Eur. Phys. J. A **47**, 44 (2011). https://doi.org/10.1140/epja/i2011-11044-1
140. N.I. Ashwood, M. Freer, S. Ahmed et al., Helium clustering in neutron-rich be isotopes. Phys. Lett. B **580**, 129–136 (2004). https://doi.org/10.1016/j.physletb.2003.11.035
141. J.E. Riley, A.M. Laird, N. de Séréville et al., Sub-threshold states in ^{19}Ne relevant to ^{18}F$(p,\alpha)^{15}$O. Phys. Rev. C **103**, 015807 (2021). https://doi.org/10.1103/PhysRevC.103.015807
142. B. Yang, Y.L. Ye, J.L. Lou et al., Spin determination by in-plane angular correlation analysis in various coordinate systems. Chin. Phys. C **43**, 084001 (2019). https://doi.org/10.1088/1674-1137/43/8/084001
143. M. Freer, J.C. Angélique, L. Axelsson et al., Helium breakup states in ^{10}Be and ^{12}Be. Phys. Rev. C **63**, 034301 (2001). https://doi.org/10.1103/PhysRevC.63.034301
144. K. Ma, Y.L. Ye, C.J. Lin et al., New measurement of ^{4}He and proton decays from resonant states in ^{19}Ne. Chin. Phys. C **47**, 114001 (2023). https://doi.org/10.1088/1674-1137/acc16f
145. E. Costanzo, M. Lattuada, S. Romano et al., A procedure for the analysis of the data of a three body nuclear reaction. Nucl. Instrum. Methods A **295**, 373–376 (1990). https://doi.org/10.1016/0168-9002(90)90715-I
146. J.X. Han, Study on the π-bond linear-chain molecular band in ^{14}C. Ph.D. thesis, Peking University (2022) (in Chinese)
147. T. Yamada, Y. Funaki, T. Myo et al., Isoscalar monopole excitations in ^{16}O: α-cluster states at low energy and mean-field-type states at higher energy. Phys. Rev. C **85**, 034315 (2012). https://doi.org/10.1103/PhysRevC.85.034315
148. G. Satchler, Isospin and macroscopic models for the excitation of giant resonances and other collective states. Nucl. Phys. A **472**, 215–236 (1987). https://doi.org/10.1016/0375-9474(87)90208-9
149. D.J. Horen, J.R. Beene, G.R. Satchler, Folded potential analysis of the excitation of giant resonances by heavy ions. Phys. Rev. C **52**, 1554–1564 (1995). https://doi.org/10.1103/PhysRevC.52.1554
150. G.R. Satchler, D.T. Khoa, Missing monopole strength in ^{58}Ni and uncertainties in the analysis of α-particle scattering. Phys. Rev. C **55**, 285–297 (1997). https://doi.org/10.1103/PhysRevC.55.285
151. M. Itoh, H. Sakaguchi, M. Uchida et al., Compressional-mode giant resonances in deformed nuclei. Phys. Lett. B **549**, 58–63 (2002). https://doi.org/10.1016/S0370-2693(02)02892-7
152. D.H. Youngblood, H.L. Clark, Y.W. Lui, Incompressibility of nuclear matter from the giant monopole resonance. Phys. Rev. Lett. **82**, 691–694 (1999). https://doi.org/10.1103/PhysRevLett.82.691
153. Z.H. Yang, Y.L. Ye, Z.H. Li et al., Helium–helium clustering states in ^{12}Be. Phys. Rev. C **91**, 024304 (2015). https://doi.org/10.1103/PhysRevC.91.024304
154. F. Ajzenberg-Selove, Energy levels of light nuclei A = 16–17. Nucl. Phys. A **460**, 1–110 (1986). https://doi.org/10.1016/0375-9474(86)90038-2
155. T. Yamada, Y. Funaki, H. Horiuchi et al., Monopole excitation to cluster states. Prog. Theor. Phys. **120**, 1139–1167 (2008). https://doi.org/10.1143/PTP.120.1139
156. J.X. Han, Y. Liu, Y.L. Ye et al., Observation of the $\pi^2\sigma^2$-bond linear-chain molecular structure in ^{16}C. Phys. Rev. C **105**, 044302 (2022). https://doi.org/10.1103/PhysRevC.105.044302

157. B. Yang, Y.L. Ye, J. Feng et al., Investigation of the ^{14}C+α molecular configuration in ^{18}O by means of transfer and sequential decay reaction. Phys. Rev. C **99**, 064315 (2019). https://doi.org/10.1103/PhysRevC.99.064315
158. D.L. Price, M. Freer, N.I. Ashwood et al., α decay of excited states in ^{14}C. Phys. Rev. C **75**, 014305 (2007). https://doi.org/10.1103/PhysRevC.75.014305
159. M. Freer, The analysis of angular correlations in breakup reactions: the effect of coordinate geometries. Nucl. Instrum. Methods A **383**, 463–472 (1996). https://doi.org/10.1016/S0168-9002(96)00866-2
160. W. Rae, R. Bhowmik, Reaction mechanism and spin information in the sequential breakup of 18O at 82 MeV. Nucl. Phys. A **420**, 320–350 (1984). https://doi.org/10.1016/0375-9474(84)90445-7
161. N. Curtis, D.D. Caussyn, N.R. Fletcher et al.,Decay angular correlations and spectroscopy for ^{10}Be$^{*}\rightarrow^{4}$He+^{6}He. Phys. Rev. C **64**, 044604 (2001). https://doi.org/10.1103/PhysRevC.64.044604
162. S.P.G. Chappell, W.D.M. Rae, Angular correlations for α-particle decay in the reaction $^{12}[^{12}$C,^{12}C$(3^{-}_{1})\rightarrow^{8}Be(0^{+}_{1})+\alpha]^{12}$C* at $E_{\mathrm{c.m.}}$=32.5 MeV. Phys. Rev. C **53**, 2879–2884 (1996). https://doi.org/10.1103/PhysRevC.53.2879
163. E. Costanzo, M. Lattuada, S. Romano et al., Excitation of ^{24}Mg states through the interaction of 85 MeV ^{16}O ions with ^{12}C and ^{24}Mg targets. Phys. Rev. C **44**, 111–118 (1991). https://doi.org/10.1103/PhysRevC.44.111
164. D. Dell'Aquila, I. Lombardo, L. Acosta et al., New experimental investigation of the structure of ^{10}Be and ^{16}C by means of intermediate-energy sequential breakup. Phys. Rev. C **93**, 024611 (2016). https://doi.org/10.1103/PhysRevC.93.024611
165. W.H. Ma, D. Patel, Y.Y. Yang et al., Observation of ^{6}He+t cluster states in ^{9}Li. Phys. Rev. C **103**, L061302 (2021). https://doi.org/10.1103/PhysRevC.103.L061302
166. N. Curtis, N.I. Ashwood, N.M. Clarke et al., Angular correlation measurements for the α+^{6}He decay of ^{10}Be. Phys. Rev. C **70**, 014305 (2004). https://doi.org/10.1103/PhysRevC.70.014305
167. S. Marsh, W. Rae, Angular correlations in heavy ion reactions. Phys. Lett. B **153**, 21–24 (1985). https://doi.org/10.1016/0370-2693(85)91433-9
168. Z.H. Yang, Y.L. Ye, Z.H. Li et al., Determination of the cluster spectroscopic factor of the 10.3 MeV state in ^{12}Be. Sci. China Phys. Mech. Astron. (2014). https://doi.org/10.1007/s11433-014-5555-5
169. P. Descouvemont, D. Baye, The R-matrix theory. Rep. Prog. Phys. **73**, 036301 (2010). https://doi.org/10.1088/0034-4885/73/3/036301
170. L.G. Sobotka, W.W. Buhro, R.J. Charity et al., Proton decay of excited states in ^{12}N and ^{13}O and the astrophysical ^{11}C$(p,\gamma)^{12}$N reaction rate. Phys. Rev. C **87**, 054329 (2013). https://doi.org/10.1103/PhysRevC.87.054329
171. A.M. Lane, R.G. Thomas, R-matrix theory of nuclear reactions. Rev. Mod. Phys. **30**, 257–353 (1958). https://doi.org/10.1103/RevModPhys.30.257
172. W.L. Pu, Y.L. Ye, J.L. Lou et al., Digital signal acquisition system for complex nuclear reaction experiments. Nucl. Sci. Tech. **35**, 12 (2024). https://doi.org/10.1007/s41365-024-01366-9
173. Y.C. Liu, X.F. Yang, S.W. Bai et al., Control and data acquisition system for collinear laser spectroscopy experiments. Nucl. Sci. Tech. **34**, 38 (2023). https://doi.org/10.1007/s41365-023-01197-0
174. H.Y. Zhu, J.L. Lou, Y.L. Ye et al., Two annular CsI(Tl) detector arrays for the charged particle telescopes. Nucl. Sci. Tech. **34**, 159 (2023). https://doi.org/10.1007/s41365-023-01319-8
175. M. Freer, J.C. Angélique, L. Axelsson et al., Exotic molecular states in ^{12}Be. Phys. Rev. Lett. **82**, 1383 (1999). https://doi.org/10.1103/PhysRevLett.82.1383
176. R.J. Charity, S.A. Komarov, L.G. Sobotka et al., Particle decay of ^{12}Be excited states. Phys. Rev. C **76**, 064313 (2007). https://doi.org/10.1103/PhysRevC.76.064313
177. T. Suhara, Y. Kanada-En'yo, Cluster structures of excited states in ^{14}C. Phys. Rev. C **82**, 044301 (2010). https://doi.org/10.1103/PhysRevC.82.044301
178. H.T. Xue, Q.B. Chen, J.W. Cui et al., Structure of low-lying states of ^{12}C and $^{13}_{\Lambda}$C in a beyond-mean-field approach. Phys. Rev. C **109**, 024324 (2024). https://doi.org/10.1103/PhysRevC.109.024324
179. W.B. He, Y.G. Ma, X.G. Cao et al., Dipole oscillation modes in light α-clustering nuclei. Phys. Rev. C **94**, 014301 (2016). https://doi.org/10.1103/PhysRevC.94.014301
180. N. Soić, M. Freer, L. Donadille et al., ^{4}He decay of excited states in ^{14}C. Phys. Rev. C **68**, 014321 (2003). https://doi.org/10.1103/PhysRevC.68.014321
181. M. Milin, S. Cherubini, T. Davinson et al., The ^{6}He scattering and reactions on ^{12}C and cluster states of ^{14}C. Nucl. Phys. A **730**, 285–298 (2004). https://doi.org/10.1016/j.nuclphysa.2003.11.011
182. D. Price, M. Freer, S. Ahmed et al., Alpha-decay of excited states in ^{13}C and ^{14}C. Nucl. Phys. A **765**, 263–276 (2006). https://doi.org/10.1016/j.nuclphysa.2005.11.004
183. P.J. Haigh, N.I. Ashwood, T. Bloxham et al., Measurement of α and neutron decay widths of excited states of ^{14}C. Phys. Rev. C **78**, 014319 (2008). https://doi.org/10.1103/PhysRevC.78.014319
184. H.L. Zang, Y.L. Ye, Z.H. Li et al., Investigation of the near-threshold cluster resonance in ^{14}C*. Chin. Phys. C **42**, 074003 (2018). https://doi.org/10.1088/1674-1137/42/7/074003
185. Z.Y. Tian, Y.L. Ye, Z.H. Li et al., Cluster decay of the high-lying excited states in ^{14}C *. Chin. Phys. C **40**, 111001 (2016). https://doi.org/10.1088/1674-1137/40/11/111001
186. H.Z. Yu, J. Li, Y.L. Ye et al., Novel evidence for the σ-bond linear-chain molecular structure in ^{14}C. Chin. Phys. C **45**, 084002 (2021). https://doi.org/10.1088/1674-1137/ac04a0
187. Z. Li, J. Zhu, T. Wang et al., Cluster structure of ^{11}C investigated with a breakup reaction. Phys. Rev. C **107**, 014320 (2023). https://doi.org/10.1103/PhysRevC.107.014320
188. J. Bishop, G.V. Rogachev, S. Ahn et al., Cluster structure of 3α + p states in ^{13}N. Phys. Rev. C **109**, 054308 (2024). https://doi.org/10.1103/PhysRevC.109.054308
189. D.T. Khoa, D.C. Cuong, Missing monopole strength of the hoyle state in the inelastic α+^{12}C scattering. Phys. Lett. B **660**, 331–338 (2008). https://doi.org/10.1016/j.physletb.2007.12.059
190. A.N. Danilov, T.L. Belyaeva, A.S. Demyanova et al., Determination of nuclear radii for unstable states in ^{12}C with diffraction inelastic scattering. Phys. Rev. C **80**, 054603 (2009). https://doi.org/10.1103/PhysRevC.80.054603
191. W. von Oertzen, Alpha-cluster condensations in nuclei and experimental approaches for their studies, (Springer, Berlin, 2010), pp. 109–128. https://doi.org/10.1007/978-3-642-13899-7_3
192. Y. Kanada-En'yo, Cluster states and monopole transitions in ^{16}O. Phys. Rev. C **89**, 024302 (2014). https://doi.org/10.1103/PhysRevC.89.024302
193. K.C.W. Li, R. Neveling, P. Adsley et al., Characterization of the proposed 4-α cluster state candidate in ^{16}O. Phys. Rev. C **95**, 031302 (2017). https://doi.org/10.1103/PhysRevC.95.031302
194. M. Freer, N.M. Clarke, N. Curtis et al., ^{8}Be and α decay of ^{16}O. Phys. Rev. C **51**, 1682–1692 (1995). https://doi.org/10.1103/PhysRevC.51.1682
195. M. Freer, M.P. Nicoli, S.M. Singer et al., ^{8}Be+^{8}Be decay of excited states in ^{16}O. Phys. Rev. C **70**, 064311 (2004). https://doi.org/10.1103/PhysRevC.70.064311

196. N. Curtis, S. Almaraz-Calderon, A. Aprahamian et al., ^{8}Be + ^{8}Be and ^{12}C+ α breakup states in ^{16}O populated via the ^{13}C(^{4}He,4α)n reaction. Phys. Rev. C **94**, 034313 (2016). https://doi.org/10.1103/PhysRevC.94.034313
197. S. Manna, T.K. Rana, C. Bhattacharya et al., Search for the hoyle analogue state in ^{16}O. Eur. Phys. J. A **57**, 286 (2021). https://doi.org/10.1140/epja/s10050-021-00592-8
198. S. Ohkubo, Y. Hirabayashi, α-particle condensate states in ^{16}O. Phys. Lett. B **684**, 127–131 (2010). https://doi.org/10.1016/j.physletb.2009.12.066
199. Y. Taniguchi, K. Yoshida, Y. Chiba et al., Unexpectedly enhanced α-particle preformation in ^{48}Ti probed by the $(p, p\alpha)$ reaction. Phys. Rev. C **103**, L031305 (2021). https://doi.org/10.1103/PhysRevC.103.L031305
200. T. Kokalova, M. Freer, N. Curtis et al., Yield measurements for resonances above the multi-α threshold in ^{20}Ne. Phys. Rev. C **87**, 057309 (2013). https://doi.org/10.1103/PhysRevC.87.057309
201. T. Kawabata, T. Adachi, M. Fujiwara et al., Search for alpha inelastic condensed state in ^{24}Mg. J. Phys. Conf. Ser. **436**, 012009 (2013). https://doi.org/10.1088/1742-6596/436/1/012009
202. M. Barbui, K. Hagel, J. Gauthier et al., Searching for states analogous to the ^{12}C hoyle state in heavier nuclei using the thick target inverse kinematics technique. Phys. Rev. C **98**, 044601 (2018). https://doi.org/10.1103/PhysRevC.98.044601
203. Y. Fujikawa, T. Kawabata, S. Adachi et al., Search for the 6α condensed state in ^{24}Mg using the ^{12}C + ^{12}C scattering. Phys. Lett. B **848**, 138384 (2024). https://doi.org/10.1016/j.physletb.2023.138384
204. X.G. Cao, E.J. Kim, K. Schmidt et al., Examination of evidence for resonances at high excitation energy in the 7α disassembly of ^{28}Si. Phys. Rev. C **99**, 014606 (2019). https://doi.org/10.1103/PhysRevC.99.014606
205. J. Bishop, T. Kokalova, M. Freer et al., Experimental investigation of α condensation in light nuclei. Phys. Rev. C **100**, 034320 (2019). https://doi.org/10.1103/PhysRevC.100.034320
206. Z.Y. Zhang, Z.G. Gan, H.B. Yang et al., New isotope ^{220}Np: probing the robustness of the N=126 shell closure in neptunium. Phys. Rev. Lett. **122**, 192503 (2019). https://doi.org/10.1103/PhysRevLett.122.192503
207. L. Ma, Z.Y. Zhang, Z.G. Gan et al., Short-lived α-emitting isotope ^{222}Np and the stability of the N = 126 magic shel. Phys. Rev. Lett. **125**, 032502 (2020). https://doi.org/10.1103/PhysRevLett.125.032502
208. Z.Y. Zhang, H.B. Yang, M.H. Huang et al., New α-emitting isotope ^{214}U and abnormal enhancement of α-particle clustering in lightest uranium isotopes. Phys. Rev. Lett. **126**, 152502 (2021). https://doi.org/10.1103/PhysRevLett.126.152502
209. Z.Y. Zhang, H.B. Yang, M.H. Huang et al., Discovery of new isotopes ^{160}Os and ^{156}W: Revealing enhanced stability of the N = 82 shell closure on the neutron-deficient side. Phys. Rev. Lett. **132**, 072502 (2024). https://doi.org/10.1103/PhysRevLett.132.072502
210. I. Tanihata, H. Savajols, R. Kanungo, Recent experimental progress in nuclear halo structure studies. Prog. Part. Nucl. Phys. **68**, 215–313 (2013). https://doi.org/10.1016/j.ppnp.2012.07.001
211. Z.X. Cao, Y.L. Ye, J. Xiao et al., Recoil proton tagged knockout reaction for ^{8}He. Phys. Lett. B **707**, 46–51 (2012). https://doi.org/10.1016/j.physletb.2011.12.009
212. D. Torresi, C. Wheldon, T. Kokalova et al., Evidence for ^{15}O+α resonance structures in ^{19}Ne via direct measurement. Phys. Rev. C **96**, 044317 (2017). https://doi.org/10.1103/PhysRevC.96.044317
213. M.L. Avila, G.V. Rogachev, V.Z. Goldberg et al., α-cluster structure of ^{18}O. Phys. Rev. C **90**, 024327 (2014). https://doi.org/10.1103/PhysRevC.90.024327
214. D. Suzuki, M. Ford, D. Bazin et al., Prototype AT-TPC: toward a new generation active target time projection chamber for radioactive beam experiments. Nucl. Instrum. Methods A **691**, 39–54 (2012). https://doi.org/10.1016/j.nima.2012.06.050
215. J.Y. Xu, Q.T. Li, Y.L. Ye et al., Performance of a small AT-TPC prototype. Nucl. Sci. Tech. **29**, 97 (2018). https://doi.org/10.1007/s41365-018-0437-6
216. L.S. Yang, J.Y. Xu, Q.T. Li et al., Performance of the AT-TPC based on two-dimensional readout strips. Nucl. Sci. Tech. **32**, 85 (2021). https://doi.org/10.1007/s41365-021-00919-6
217. E. Koshchiy, G. Rogachev, E. Pollacco et al., Texas active target (texat) detector for experiments with rare isotope beams. Nucl. Instrum. Methods A **957**, 163398 (2020). https://doi.org/10.1016/j.nima.2020.163398
218. J. Hooker, G.V. Rogachev, E. Koshchiy et al., Structure of ^{9}C through proton resonance scattering with the texas active target detector. Phys. Rev. C **100**, 054618 (2019). https://doi.org/10.1103/PhysRevC.100.054618
219. M. Barbui, A. Volya, E. Aboud et al., α-cluster structure of ^{18}Ne. Phys. Rev. C **106**, 054310 (2022). https://doi.org/10.1103/PhysRevC.106.054310
220. M. Heffner, D. Asner, R. Baker et al., A time projection chamber for high accuracy and precision fission cross-section measurements. Nucl. Instrum. Methods A **759**, 50–64 (2014). https://doi.org/10.1016/j.nima.2014.05.057
221. T. Wakasa, K. Ogata, T. Noro, Proton-induced knockout reactions with polarized and unpolarized beams. Prog. Part. Nucl. Phys. **96**, 32–87 (2017). https://doi.org/10.1016/j.ppnp.2017.06.002
222. T. Aumann, C. Barbieri, D. Bazin et al., Quenching of single-particle strength from direct reactions with stable and rare-isotope beams. Prog. Part. Nucl. Phys. **118**, 103847 (2021). https://doi.org/10.1016/j.ppnp.2021.103847
223. P.G. Roos, N.S. Chant, A.A. Cowley et al., Absolute spectroscopic factors from the (p, pα) reaction at 100 MeV on 1p-shell nuclei. Phys. Rev. C **15**, 69–83 (1977). https://doi.org/10.1103/PhysRevC.15.69
224. T.A. Carey, P.G. Roos, N.S. Chant et al., Alpha-clustering systematics from the quasifree $(p, p\alpha)$ knockout reaction. Phys. Rev. C **23**, 576–579 (1981). https://doi.org/10.1103/PhysRevC.23.576
225. T.A. Carey, P.G. Roos, N.S. Chant et al., Alpha-particle spectroscopic strengths using the $(p, p\alpha)$ reaction at 101.5 MeV. Phys. Rev. C **29**, 1273–1288 (1984). https://doi.org/10.1103/PhysRevC.29.1273
226. M.J. Lyu, K. Yoshida, Y. Kanada-En'yo et al., Manifestation of α clustering in ^{10}Be via α-knockout reaction. Phys. Rev. C **97**, 044612 (2018). https://doi.org/10.1103/PhysRevC.97.044612
227. K. Yoshida, Y. Chiba, M. Kimura et al., Quantitative description of the ^{20}Ne(p, $p\alpha$) ^{16}O reaction as a means of probing the surface α amplitude. Phys. Rev. C **100**, 044601 (2019). https://doi.org/10.1103/PhysRevC.100.044601
228. X. Roca-Maza, N. Paar, Nuclear equation of state from ground and collective excited state properties of nuclei. Prog. Part. Nucl. Phys. **101**, 96–176 (2018). https://doi.org/10.1016/j.ppnp.2018.04.001
229. M. Kimura, T. Suhara, Y. Kanada-En'yo, Antisymmetrized molecular dynamics studies for exotic clustering phenomena in neutron-rich nuclei. Eur. Phys. J. A **52**, 1273–1288 (2016). https://doi.org/10.1140/epja/i2016-16373-9
230. Y. Kanada-En'yo, H. Horiuchi, Coexistence of cluster and shell-model aspects in nuclear systems. Front. Phys. **13**, 132108 (2018). https://doi.org/10.1007/s11467-018-0830-y
231. P.J. Li, D. Beaumel, J. Lee et al., Validation of the ^{10}Be ground-state molecular structure using ^{10}Be($p, p\alpha$)^{6}He triple differential reaction cross-section measurements. Phys. Rev. Lett. **131**, 212501 (2023). https://doi.org/10.1103/PhysRevLett.131.212501

232. Y. Kanada-En'yo, Proton radii of Be, B, and C isotopes. Phys. Rev. C **91**, 014315 (2015). https://doi.org/10.1103/PhysRevC.91.014315
233. Y. Chen, Y.L. Ye, K. Wei, Progress and perspective of the research on exotic structures of unstable nuclei. Nucl. Tech **46**, 189–194 (2023). https://doi.org/10.11889/j.0253-3219.2023.hjs.46.080020
234. H. Hua, Y.L. Ye, X.F. Yang, Advancements in nuclear physics research using Beijing HI-13 tandem accelerator. Nucl. Tech. **46**, 51–62 (2023). https://doi.org/10.11889/j.0253-3219.2023.hjs.46.080004
235. H. Pais, R. Bougault, F. Gulminelli et al., Low density in-medium effects on light clusters from heavy-ion data. Phys. Rev. Lett. **125**, 012701 (2020). https://doi.org/10.1103/PhysRevPhysRevLett.125.012701
236. W. Broniowski, E. Ruiz-Arriola, Signatures of α clustering in light nuclei from relativistic nuclear collisions. Phys. Rev. Lett. **112**, 112501 (2014). https://doi.org/10.1103/PhysRevPhysRevLett.112.112501
237. W. Horiuchi, N. Itagaki, Imprints of α clustering in the density profiles of ^{12}C and ^{16}O. Phys. Rev. C **107**, L021304 (2023). https://doi.org/10.1103/PhysRevC.107.L021304
238. Y.X. Watanabe, Y.H. Kim, S.C. Jeong et al., Pathway for the production of neutron-rich isotopes around the $N = 126$ shell closure. Phys. Rev. Lett. **115**, 172503 (2015). https://doi.org/10.1103/PhysRevLett.115.172503
239. F. Galtarossa, L. Corradi, S. Szilner et al., Mass correlation between light and heavy reaction products in multinucleon transfer ^{197}Au + ^{130}Te collisions. Phys. Rev. C **97**, 054606 (2018). https://doi.org/10.1103/PhysRevC.97.054606
240. E.M. Kozulin, G.N. Knyazheva, A.V. Karpov et al., Detailed study of multinucleon transfer features in the ^{136}Xe + ^{238}U reaction. Phys. Rev. C **109**, 034616 (2024). https://doi.org/10.1103/PhysRevC.109.034616
241. J.G. Li, N. Michel, W. Zuo et al., Unbound spectra of neutron-rich oxygen isotopes predicted by the Gamow Shell model. Phys. Rev. C **103**, 034305 (2021). https://doi.org/10.1103/PhysRevC.103.034305
242. J. Tanaka, R. Tsuji, K. Higuchi et al., Designing togaxsi: telescope for inverse-kinematics cluster-knockout reactions. Nucl. Instrum. Methods B **542**, 4–6 (2023). https://doi.org/10.1016/j.nimb.2023.05.054
243. S. Typel, G. Röpke, T. Klähn et al., Composition and thermodynamics of nuclear matter with light clusters. Phys. Rev. C **81**, 015803 (2010). https://doi.org/10.1103/PhysRevC.81.015803
244. Z.W. Zhang, L.W. Chen, Low density nuclear matter with light clusters in a generalized nonlinear relativistic mean-field model. Phys. Rev. C **95**, 064330 (2017). https://doi.org/10.1103/PhysRevC.95.064330
245. T. Uesaka, N. Itagaki, Nuclear clustering-manifestations of non-uniformity in nuclei. Philos. Trans. R. Soc. A **382**, 20230123 (2024). https://doi.org/10.1098/rsta.2023.0123